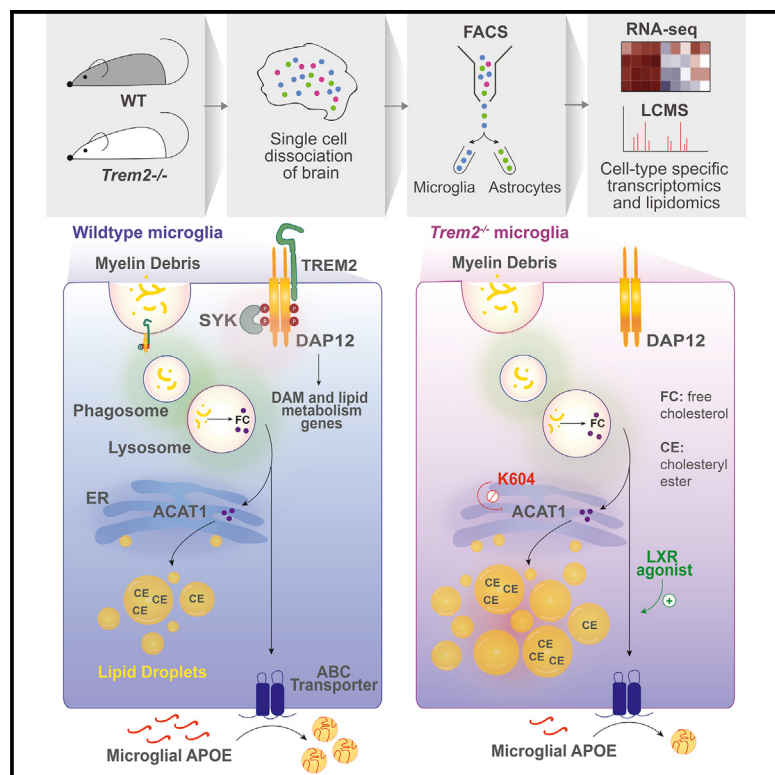


# TREM2 Regulates Microglial Cholesterol Metabolism upon Chronic Phagocytic Challenge

## Graphical Abstract



## Authors

Alicia A. Nugent, Karin Lin,  
Bettina van Lengerich, ...,  
Joseph W. Lewcock,  
Kathryn M. Monroe, Gilbert Di Paolo

## Correspondence

monroe@dnli.com (K.M.M.),  
dipaolo@dnli.com (G.D.P.)

## In Brief

TREM2 and APOE are implicated in late-onset Alzheimer's disease. Here, Nugent et al. report that TREM2 upregulates *Apoe* and other damage-associated microglial genes upon chronic demyelination. Loss of either *Trem2* or *Apoe* causes dysregulated cholesterol transport and metabolism in microglia.

## Highlights

- Upon demyelination, *Trem2*<sup>-/-</sup> microglia fail to upregulate lipid metabolism genes
- Trem2*<sup>-/-</sup> microglia accumulate cholestryly ester derived from myelin cholesterol
- Accumulation is rescued by ACAT1 inhibitor and LXR agonist
- Apoe*<sup>-/-</sup> glia defective in cholesterol transport also accumulate cholestryly ester

# TREM2 Regulates Microglial Cholesterol Metabolism upon Chronic Phagocytic Challenge

Alicia A. Nugent,<sup>1,2</sup> Karin Lin,<sup>1,2</sup> Bettina van Lengerich,<sup>1</sup> Steve Lianoglou,<sup>1</sup> Laralynne Przybyla,<sup>1</sup> Sonnet S. Davis,<sup>1</sup> Ceyda Llapashtica,<sup>1</sup> Junhua Wang,<sup>1</sup> Do Jin Kim,<sup>1</sup> Dan Xia,<sup>1</sup> Anthony Lucas,<sup>1</sup> Sulochanadevi Baskaran,<sup>1,3</sup> Patrick C.G. Haddick,<sup>1</sup> Melina Lenser,<sup>1</sup> Timothy K. Earr,<sup>1</sup> Ju Shi,<sup>1,4</sup> Jason C. Dugas,<sup>1</sup> Benjamin J. Andreone,<sup>1</sup> Todd Logan,<sup>1</sup> Hilda O. Solanoy,<sup>1</sup> Hang Chen,<sup>1,5</sup> Ankita Srivastava,<sup>1</sup> Suresh B. Poda,<sup>1</sup> Pascal E. Sanchez,<sup>1</sup> Ryan J. Watts,<sup>1</sup> Thomas Sandmann,<sup>1</sup> Giuseppe Astarita,<sup>1</sup> Joseph W. Lewcock,<sup>1</sup> Kathryn M. Monroe,<sup>1,\*</sup> and Gilbert Di Paolo<sup>1,6,\*</sup>

<sup>1</sup>Denali Therapeutics, South San Francisco, CA 94080, USA

<sup>2</sup>These authors contributed equally

<sup>3</sup>Current address: Frontier Medicines, South San Francisco, CA 94080, USA

<sup>4</sup>Current address: Jazz Pharmaceuticals, Palo Alto, CA 94304, USA

<sup>5</sup>Current address: BridGene Biosciences, Sunnyvale, CA 94089, USA

<sup>6</sup>Lead Contact

\*Correspondence: [monroe@dnli.com](mailto:monroe@dnli.com) (K.M.M.), [dipaolo@dnli.com](mailto:dipaolo@dnli.com) (G.D.P.)

<https://doi.org/10.1016/j.neuron.2019.12.007>

## SUMMARY

Loss-of-function (LOF) variants of TREM2, an immune receptor expressed in microglia, increase Alzheimer's disease risk. TREM2 senses lipids and mediates myelin phagocytosis, but its role in microglial lipid metabolism is unknown. Combining chronic demyelination paradigms and cell sorting with RNA sequencing and lipidomics, we find that wild-type microglia acquire a disease-associated transcriptional state, while TREM2-deficient microglia remain largely homeostatic, leading to neuronal damage. TREM2-deficient microglia phagocytose myelin debris but fail to clear myelin cholesterol, resulting in cholesterol ester (CE) accumulation. CE increase is also observed in APOE-deficient glial cells, reflecting impaired brain cholesterol transport. This finding replicates in myelin-treated TREM2-deficient murine macrophages and human iPSC-derived microglia, where it is rescued by an ACAT1 inhibitor and LXR agonist. Our studies identify TREM2 as a key transcriptional regulator of cholesterol transport and metabolism under conditions of chronic myelin phagocytic activity, as TREM2 LOF causes pathogenic lipid accumulation in microglia.

## INTRODUCTION

Microglia constantly surveil the brain parenchyma to eliminate dead cells, dysfunctional synapses, and other cellular debris (Deczkowska et al., 2018; Hammond et al., 2018; Ransohoff, 2016). With aging or in pathological conditions, parenchyma damage can facilitate the transition of microglia from homeostatic into reactive states. This transition profoundly alters the microglial transcriptome, leading to morphological changes, increased phagocytic activity, expression of various immune re-

ceptors, and enhanced cytokine secretion (Deczkowska et al., 2018; Hammond et al., 2018). Recent advances in single-cell RNA sequencing (scRNA-seq) have revealed multiple states of microglia. These studies suggest that functional sub-populations of microglia co-exist within the brain in various mouse models of neurodegenerative diseases, including homeostatic and disease-associated microglia (DAM), the microglial neurodegenerative phenotype (MGnD), and activated response microglia (ARM) (Deczkowska et al., 2018; Keren-Shaul et al., 2017; Krasemann et al., 2017; Sala Frigerio et al., 2019). Collectively, we refer to responsive microglial states as damage-associated microglia, because different disease or aging models show significant overlap but distinct transcriptional profiles. Whether transition to damage-associated microglia states is beneficial or deleterious remains unclear and likely depends on the disease type, stage, and inherent pathology. Identifying the molecular and cellular basis underlying microglial states in healthy and disease conditions may facilitate the development of immune therapies for the treatment of neurodegenerative diseases.

Microglial dysfunction appears central to the etiology of late-onset Alzheimer's disease (LOAD), as large-scale genetic studies have uncovered variants in LOAD risk-associated genes that are highly expressed in microglia (Carmona et al., 2018; Efthymiou and Goate, 2017). One of the LOAD genes encodes triggering receptor expressed on myeloid cells 2 (TREM2), a single-pass transmembrane immune receptor selectively expressed in microglia within the CNS. Individuals carrying rare heterozygous variants of TREM2, such as R47H, have higher LOAD risk (average odds ratio [OR] ~4.5) (Guerreiro et al., 2013; Jonsson et al., 2013; Ulland and Colonna, 2018). The immunoglobulin-like ectodomain (ECD) of TREM2 binds various ligands, including lipids, and the AD variant R47H has reduced affinity for apolipoproteins (e.g., APOE) or lipid ligands, suggesting that the increased LOAD risk reflects a partial loss of function (LOF) in lipid recognition and/or lipid-induced signaling (Atagi et al., 2015; Bailey et al., 2015; Sudom et al., 2018; Ulland and Colonna, 2018; Wang et al., 2016; Yeh et al., 2016). *Trem2*<sup>-/-</sup> and *Trem2*<sup>R47H</sup> mutant microglia fail to surround and clear amyloid plaques *in vivo*, resulting in accumulation of dystrophic

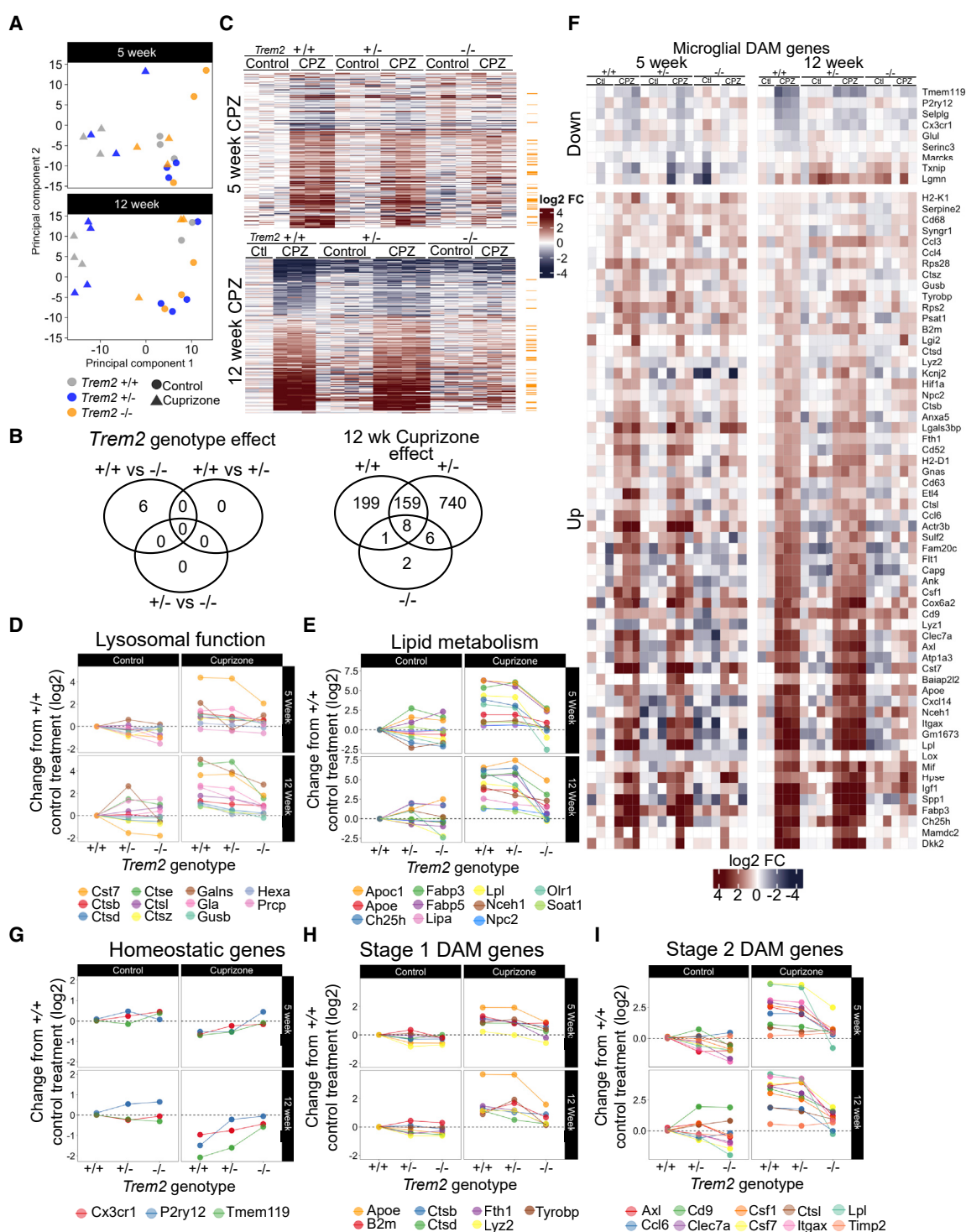


**Figure 1. TREM2 Deficiency Prevents DAM Conversion during Chronic Demyelination**

(A) Principal-component analysis of top 500 differentially expressed genes in bulk microglia isolated from brains of control versus 5 week and control versus 12 week cuprizone (CPZ)-treated *Trem2*<sup>+/+</sup>, *Trem2*<sup>+/-</sup>, and *Trem2*<sup>-/-</sup> mice (n = 2–4 mice per condition).

(B) Number of differentially expressed genes in bulk microglia after control (left) or 12 week CPZ diet (right). ANOVA; FDR < 0.1; absolute  $\log_2$  FC > 0.5.

(C) Heatmap of top gene expression changes ( $\log_2$  fold change) in bulk microglia after 5 (top) and 12 (bottom) week CPZ diet. Orange marks indicate previously identified DAM genes. ANOVA, FDR < 0.1, absolute  $\log_2$  FC > 0.5;

(legend continued on next page)

neurites near diffuse plaques (Jay et al., 2017; Parhizkar et al., 2019; Ulland and Colonna, 2018; Wang et al., 2015, 2016; Yuan et al., 2016). Additionally, TREM2 LOF modulates tau seeding, spreading, and tau-associated neuroinflammation and neurotoxicity (Bemiller et al., 2017; Leyns et al., 2017, 2019; Sayed et al., 2018). *Trem2* overexpression reduces amyloid burden and neuritic dystrophy in an Alzheimer's disease (AD) mouse model (Lee et al., 2018). Rare homozygous *TREM2* LOF mutations cause Nasu-Hakola disease, a syndrome with recurrent bone fractures, myelin loss, neurodegeneration, and early-onset dementia, likely resulting from microglial dysfunction (Paloneva et al., 2002).

Consistent with a role in microglia proliferation and survival, TREM2 signals via receptor tyrosine kinases DNAX-activation protein 10 (DAP10) and DAP12 to modulate proliferation, survival, immune response, calcium mobilization, cytoskeletal dynamics, mTOR signaling, autophagy, and energy metabolism (Ulland and Colonna, 2018; Ulland et al., 2017; Yeh et al., 2017). A proposed function of TREM2 is to mediate microglial response and transition to a damage-associated microglia state via control of gene expression (Deczkowska et al., 2018; Ulland and Colonna, 2018). scRNA-seq analyses of TREM2-deficient 5XFAD microglia revealed the inability to acquire a late-stage DAM profile (DAM stage 2), instead halting at an intermediate DAM state (DAM stage 1) (Keren-Shaul et al., 2017). Other studies showed a key role for TREM2 and APOE in the transition to damage-associated microglia states (Krasemann et al., 2017; Götzl et al., 2019). Microarray studies in *Trem2*<sup>-/-</sup> mice subjected to a demyelinating cuprizone (CPZ) diet also showed that TREM2 controls expression of many microglial genes controlling lipid transport (*Apoe*) or catabolism (*Lp*) (Poliani et al., 2015). *Trem2*<sup>-/-</sup> mice showed normal demyelination in the acute phase but partial remyelination during the recovery phase, suggesting that TREM2 may bind to myelin debris for engulfment and clearance, a process required for proper remyelination (Cantoni et al., 2015; Poliani et al., 2015). However, whether TREM2 mediates myelin lipid processing in microglia is unknown.

We sought to assess the physiological role of TREM2 in microglial lipid metabolism by subjecting mice to a demyelinating CPZ diet (Praet et al., 2014). Myelin contains the majority (>80%) of the brain's free cholesterol (Martín et al., 2014), allowing the assessment of microglial response to a chronic and extensive cholesterol challenge that is selective to the brain and independent of peripheral lipid metabolism. CPZ triggered the TREM2-dependent transition from a homeostatic to damage-associated microglia state with upregulation of genes controlling lipid transport and metabolism. Chronic myelin phagocytosis caused accumulation of cholesteryl ester (CE) and oxidized CE (oxCE) in *Trem2*<sup>-/-</sup> brain. Fluorescence-activated cell sorting (FACS)-based

lipidomic techniques revealed elevation of CE in *Trem2*<sup>-/-</sup> microglia, a phenotype also observed in *Apoe*<sup>-/-</sup> microglia after CPZ diet. This could be reproduced *in vitro*, where CE accumulation occurs in *Trem2*<sup>-/-</sup> bone marrow-derived macrophages (BMDMs) and human induced pluripotent stem cell (iPSC)-derived microglia subjected to myelin challenge. CE accumulation was rescued by inhibition of acetyl-CoA acetyltransferase 1 (ACAT1), which converts cholesterol to CE, and by a liver X receptor (LXR) agonist, suggesting that TREM2 LOF causes an impairment in cholesterol efflux. Our results establish a key role for TREM2 in the control of microglial gene expression and cholesterol transport upon chronic myelin phagocytosis. Failure to properly execute this program results in extensive neuronal damage in the brain. Because CE is known to accumulate in AD patient brain and AD mouse models (Astarita et al., 2011; Chan et al., 2012; Morel et al., 2013; Shibuya et al., 2015), and LOAD-linked *TREM2* variants result in a partial LOF (Ulland and Colonna, 2018), our study strongly suggests that enhancing TREM2 function may be beneficial in AD, in part by facilitating lipid clearance in microglia.

## RESULTS

### TREM2 Deficiency Prevents DAM Conversion during Chronic Demyelination

To characterize the effects of acute and chronic demyelination on TREM2-dependent gene expression in microglia, *Trem2*<sup>+/+</sup>, *Trem2*<sup>+/-</sup>, and *Trem2*<sup>-/-</sup> mice were fed a 0.2% CPZ diet for 5 or 12 weeks. CD11b<sup>+</sup> microglia were isolated from hemibrain using FACS (Figures S1A–S1E). CPZ induced transcriptional changes in *Trem2*<sup>+/+</sup> and *Trem2*<sup>+/-</sup> microglia, whereas CPZ-challenged *Trem2*<sup>-/-</sup> microglia clustered with those of untreated mice (principal-component analysis [PCA]; Figure 1A). Few genotype-dependent differences were found under normal diet conditions (Figure 1B), but CPZ caused significant changes in hundreds of genes after 5 and 12 weeks (Figures 1B and 1C; absolute log<sub>2</sub> fold change [FC] > 0.5, false discovery rate [FDR] < 0.2; Data S1). These changes were restricted primarily to *Trem2*<sup>+/+</sup> and *Trem2*<sup>+/-</sup> microglia, while *Trem2*<sup>-/-</sup> microglia largely failed to respond to CPZ (Figures 1B and 1C).

Analysis of gene sets from the Reactome database (Fabregat et al., 2018) revealed *Trem2*-dependent upregulation of genes involved in lysosome and phagosome function, AD, oxidative phosphorylation, and cholesterol metabolism. Key lysosome cathepsin genes, such as *Ctse* and *Ctsl*, were upregulated 2-fold upon chronic demyelination in *Trem2*<sup>+/+</sup> and *Trem2*<sup>+/-</sup> microglia (FDR < 0.05) but unchanged in *Trem2*<sup>-/-</sup> microglia (Figure 1D; Data S1; interaction p < 0.05). Previous microarray studies reported a failure of *Trem2*<sup>-/-</sup> microglia to upregulate

(D and E) Expression changes in individual genes associated with (D) lysosomal function and (E) lipid metabolism in bulk microglia with control (left inset) or CPZ diet (right inset) for 5 (top) or 12 (bottom) weeks.

(F) Heatmap of bulk microglial expression changes in the top 69 DAM genes downregulated (top) or upregulated (bottom) in 5XFAD compared with wild-type microglia from Keren-Shaul et al. 2017 after 5 and 12 week control versus CPZ diet. Camera; p < 1 × 10<sup>-41</sup>.

(G–I) Expression changes in individual (G) homeostatic, (H) stage 1, and (I) stage 2 DAM genes (identified in Keren-Shaul et al., 2017) in *Trem2*<sup>+/+</sup>, *Trem2*<sup>+/-</sup>, and *Trem2*<sup>-/-</sup> bulk microglia with control (left inset) or CPZ diet (right inset) for 5 (top) or 12 (bottom) weeks.

See also Figure S1 and Data S1.

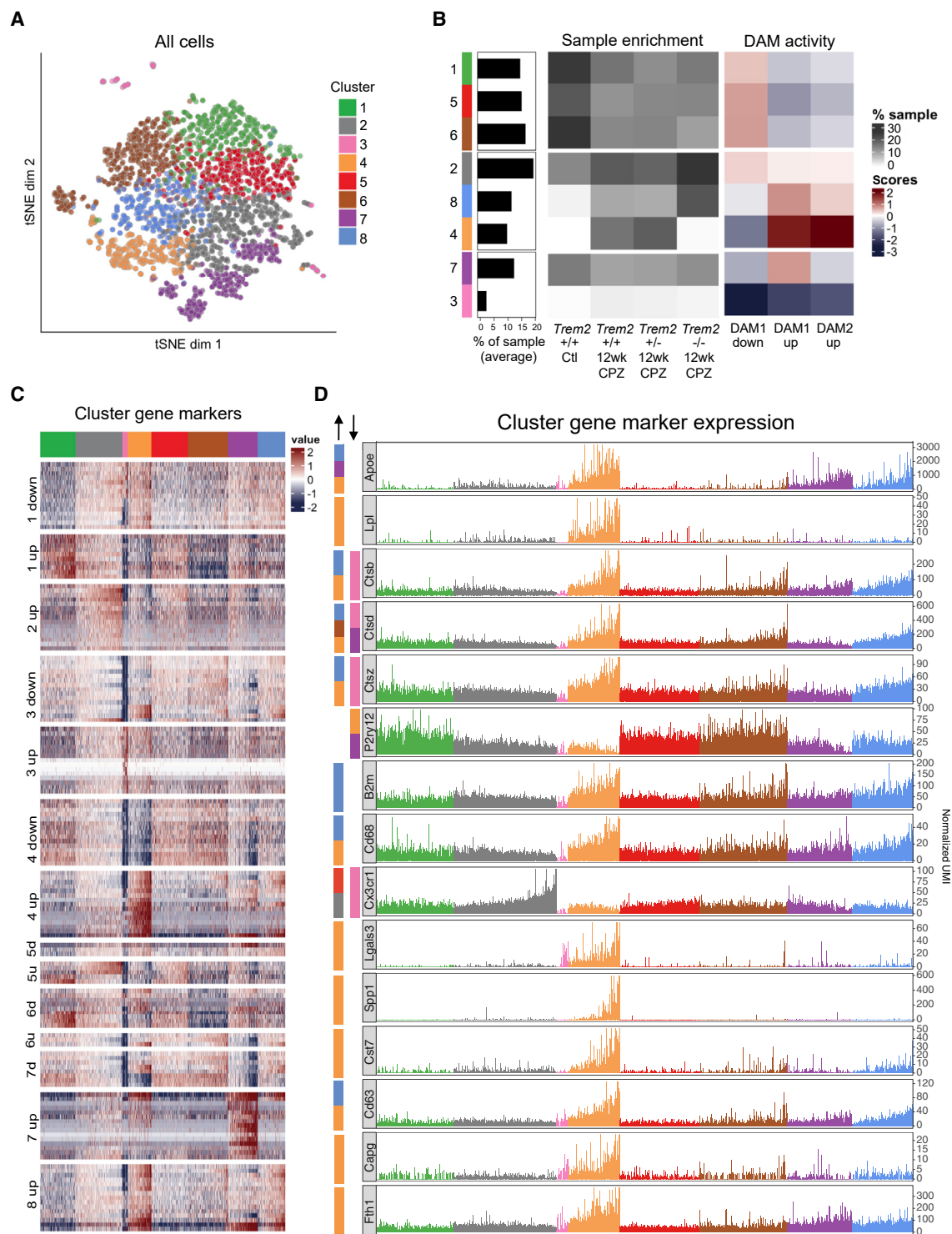


**Figure 2. scRNA-Seq Confirms that *Trem2*<sup>-/-</sup> Microglia Exhibit Attenuated Transition to DAM upon Demyelination**

(A) tSNE (t-distributed stochastic neighbor embedding) plot of the 3,023 single microglia sorted from *Trem2*<sup>+/+</sup> with control diet and *Trem2*<sup>+/+</sup>, *Trem2*<sup>+/-</sup>, and *Trem2*<sup>-/-</sup> with 12 week CPZ, colored by cluster assignment ( $n = 2$  pooled mice per condition).

(B) Percentage composition of all cells within each cluster across all samples (left), within each cluster per condition (middle), and aggregated scores of DAM-related gene sets per cluster (right). Gene set scores per cell are normalized to zero mean and unit variance and visualized in the heatmap as their average over all cells per cluster.

(legend continued on next page)

genes involved in phagocytosis and lipid metabolism (Poliani et al., 2015). We confirmed these results and expanded the list of lipid metabolism-related genes (Figure 1E). Importantly, several *Trem2*-dependent genes control cholesterol transport and metabolism, including *Apoe*, *Apoc1*, *Ch25h*, *Lipa*, *Nceh1*, *Npc2*, and *Soat1*. Gene set enrichment analysis also showed that DAM genes (Keren-Shaul et al., 2017) were significantly upregulated with CPZ in *Trem2<sup>+/+</sup>* and *Trem2<sup>+/-</sup>* microglia at both time points but attenuated in *Trem2<sup>-/-</sup>* microglia (Figures 1C, 1F, and S1F). This suggests that chronic demyelination induces expression changes related to those observed in 5XFAD and SOD1 microglia (Keren-Shaul et al., 2017).

Keren-Shaul et al. (2017) described the microglial transition from homeostasis into DAM as a two-step process: a TREM2-independent transition to DAM stage 1, followed by a TREM2-dependent transition to DAM stage 2. We compared our TREM2 CPZ dataset with published homeostatic, DAM 1, and DAM 2 gene profiles. Homeostatic genes *P2ry12* and *Tmem119* were significantly downregulated in *Trem2<sup>+/+</sup>* and *Trem2<sup>+/-</sup>* (FDR < 0.01) but not *Trem2<sup>-/-</sup>* microglia in response to CPZ (Figure 1G; genotype-diet interaction p < 0.05; Data S1). Although described as a TREM2-independent phenomenon in an AD model, we observed reduced induction of DAM 1 genes such as *Apoe* (interaction p < 0.001) and *Fth1* (interaction p < 0.005) in *Trem2<sup>-/-</sup>* compared with *Trem2<sup>+/+</sup>* and *Trem2<sup>+/-</sup>* microglia following CPZ treatment (Figure 1H). *Apoe* expression was 8-fold higher with CPZ treatment of *Trem2<sup>+/+</sup>* and *Trem2<sup>+/-</sup>* mice after 12 weeks but was attenuated in *Trem2<sup>-/-</sup>* mice, similar to DAM 2 genes, such as *Ax1* (interaction p < 0.05) and *Cd9* (interaction p < 0.001) (Figure 1I; Data S1). Our data indicate a role of TREM2 in endolysosomal function and lipid metabolism, with a clear implication of cholesterol transport and metabolism. Additionally, they suggest that CPZ elicits a damage-associated microglia state that fails to be initiated in *Trem2<sup>-/-</sup>* microglia.

### TREM2 Deficiency Reduces Age-Dependent Conversion to DAM

Microglial dysfunction is a hallmark of the aging brain, as cells accumulate excessive myelin debris and acquire a DAM transcriptional state (Mecca et al., 2018; Safaiyan et al., 2016; Keren-Shaul et al., 2017). We sorted microglia derived from young (2-month-old) and aged (15- to 17-month-old) wild-type and *Trem2<sup>-/-</sup>* mice to assess whether aged *Trem2<sup>-/-</sup>* microglia exhibit a DAM-like state. Aged wild-type microglia downregulated a number of homeostatic genes and upregulated DAM 1 and DAM 2 genes compared to young microglia, albeit to a lesser degree than modulation in the CPZ model (Figures S1G and S1H). As with CPZ, activation of the DAM 2 gene set was attenuated in aged *Trem2<sup>-/-</sup>* microglia compared with aged controls (Figures S1G and S1H). This effect was most striking for *Lpl* and *Spp1*, consistent with the *Trem2* dependency of the DAM 2 profile exhibited in 5XFAD microglia (Keren-Shaul et al.,

2017). Unlike with CPZ, microglia from aged mice only showed a mild increase in expression of cholesterol metabolism-related genes compared with young mice, suggesting that aged microglia face only a minor cholesterol burden. Thus, gene expression changes in microglia derived from CPZ-challenged *Trem2<sup>-/-</sup>* mice are also present in aged *Trem2<sup>-/-</sup>* microglia, although the latter are less striking.

### scRNA-Seq Confirms that *Trem2<sup>-/-</sup>* Microglia Exhibit Attenuated Transition to DAM upon Demyelination

To determine if the population-based CPZ-induced transcriptional changes observed were homogeneous across microglia, we conducted scRNA-seq on CD11b<sup>+</sup>/CD45<sup>low</sup> microglia isolated from CPZ-treated mice (Figures S2A–S2D). We used a graph-based clustering approach (Xu and Su, 2015) to divide 3,023 cells into eight microglia sub-populations (Figure 2A), each accounting for 2%–19% of analyzed cells (Figure 2B, left). Quantification of cluster membership across groups (Figure 2B, middle) identified two treatment- and genotype-dependent clusters (4 and 8). Cluster 4 mainly contained microglia exposed to CPZ with at least one copy of *Trem2* (~1% of *Trem2<sup>+/+</sup>* controls; 16%–19% of *Trem2<sup>+/+</sup>* CPZ and *Trem2<sup>+/-</sup>* CPZ; ~1.5% of *Trem2<sup>-/-</sup>* CPZ). Microglia from cluster 8 were largely absent in *Trem2<sup>+/+</sup>* controls (< 2.3%), mildly increased in the *Trem2<sup>+/+</sup>* CPZ and *Trem2<sup>+/-</sup>* CPZ mice (~10%), and most abundant in the *Trem2<sup>-/-</sup>* CPZ mice (~20%) (Data S2). Cluster 3 consists of very few cells and is discussed in STAR Methods.

To further characterize cells within each cluster, we identified marker genes with cluster-specific over- and under-expression (Data S2). Relative expression of the top 15 up- and downregulated genes per cluster confirmed that these clusters are distinct (Figure 2C), although genes exclusive to a single cluster are rare. Consistent with bulk RNA-seq data, the top upregulated marker genes in the *Trem2<sup>+/+</sup>* CPZ and *Trem2<sup>+/-</sup>* CPZ-enriched cluster 4 are lysosomal genes (e.g., *Ctsb*, *Ctsd*, *Ctsz*) and genes involved in lipid metabolism (e.g., *Apoe*, *Lpl*) (Figure 2D). The downregulated marker genes in cluster 4 include homeostatic genes, such as *P2ry12* and *Tmem119*, suggesting microglia in this cluster are in a reactive state (Figures 2D and S2E). Cluster 8 similarly consisted of cells with upregulated lysosome- and lipid metabolism-related genes, such as *Ctsb*, *Ctsd*, and *Apoe*, but their expression was lower than that seen in cluster 4 (Figures 2D and S2F). About 20% of the total microglia population upregulate the above genes; thus not all *Trem2<sup>+/+</sup>* and *Trem2<sup>+/-</sup>* microglia alter gene expression with CPZ.

Consistent with our bulk microglial findings, the transcriptome from *Trem2<sup>+/+</sup>* and *Trem2<sup>+/-</sup>* CPZ cluster 4 largely contained upregulated marker genes that previously have been characterized in DAM 2 expression (Keren-Shaul et al., 2017), including *Lgals3*, *Cd63*, *Spp1*, *Cst7*, *Cd68*, *Capg*, and *Fth1* (Figure 2D). To determine if clusters 4 and 8 relate to DAM stages, we aggregated the expression of established DAM stage 1 and 2 marker genes

(C) Heatmap showing the relative gene expression profiles (normalized to zero mean and unit variance) of the top 15 up- and downregulated genes per cluster.  
(D) Expression profiles for selected marker genes plotted as normalized counts per cell. Left legend denotes upregulated (up arrow) versus downregulated (down arrow) marker genes in indicated clusters.

See also Figure S2 and Data S2.

(Data S2) for each cluster. Cluster 4 showed the highest enrichment for DAM 2 gene expression, followed by cluster 8 (Figure 2B, right), suggesting that *Trem2<sup>+/+</sup>* CPZ and *Trem2<sup>+/-</sup>* CPZ microglia exhibit a DAM 2-like transition in response to CPZ that is attenuated in *Trem2<sup>-/-</sup>* CPZ microglia. As in Keren-Shaul et al. (2017), DAM 1 genes were upregulated in *Trem2<sup>+/+</sup>* CPZ, *Trem2<sup>+/-</sup>* CPZ, and *Trem2<sup>-/-</sup>* CPZ microglia, although *Trem2<sup>-/-</sup>* showed reduced upregulation. Thus, upon chronic demyelination, *Trem2<sup>-/-</sup>* microglia appear to be arrested in their transition to expression states seen in *Trem2<sup>+/+</sup>* and *Trem2<sup>+/-</sup>* microglia and are unable to upregulate transcription of DAM genes, including lysosome- and lipid metabolism-related genes, similar to reports of *Trem2<sup>-/-</sup>:5XFAD* microglia (Keren-Shaul et al., 2017). Proper conversion to reactive states during chronic demyelination may enable lysosomal degradation and/or efflux of myelin lipids.

### TREM2 Deficiency Causes Neuronal Damage during Chronic Demyelination

Neurite dystrophy occurs in CPZ-treated *Trem2<sup>-/-</sup>* mice (Cantoni et al., 2015; Poliani et al., 2015). Likewise, we found accumulation of dystrophic APP-positive puncta in the hippocampus and corpus callosum of *Trem2<sup>-/-</sup>* mice after 5 or 12 weeks of CPZ (Figures S3A and S3B). Quantification of APP-positive dystrophic neurite puncta number, intensity, or area showed a significant interaction between genotype and treatment for the 5 and/or 12 week CPZ diet (Figure S3C). Accordingly, plasma neurofilament-light chain (Nf-L) levels were higher in CPZ-treated *Trem2<sup>-/-</sup>* mice (Figure 3A; 12 week CPZ treatment-genotype interaction  $p < 0.001$ , two-way ANOVA). Similarly, aged *Trem2<sup>-/-</sup>* plasma showed higher Nf-L levels (Figure S3D; age-genotype interaction  $p < 0.05$ , two-way ANOVA), indicating that TREM2 is neuroprotective.

### TREM2 Deficiency Causes CE Accumulation in the Brain

Lipid metabolism-related genes are strongly induced upon chronic demyelination in wild-type but not *Trem2<sup>-/-</sup>* microglia (Figures 1E and 2D), including seven genes coding for proteins directly involved in cholesterol transport (*Apoe*, *Apoc1*), hydrolysis of CE in lysosomes (*Lipa*), egress of cholesterol from lysosomes (*Npc2*), CE synthesis and storage in lipid droplets (*Soat1*), CE hydrolysis in lipid droplets (*Nceh1*), and 25-hydroxylation (*Ch25h*). Thus, both intracellular and extracellular cholesterol transport may be defective in *Trem2<sup>-/-</sup>* microglia with CPZ. To test this, we conducted liquid chromatography-mass spectrometry (LCMS) analysis of lipids from coronal forebrain sections containing the corpus callosum. Brain lipidomic profiles of the three genotypes under control diet were similar (Figure 3B; Data S3). Upon 5 week CPZ, minimal changes were detected, with an enhancement in CE and oxCE levels in all three genotypes (Figure S3E). With 12 week CPZ, CE and oxCE lipid species were significantly elevated in *Trem2<sup>-/-</sup>* brain compared with *Trem2<sup>+/+</sup>* and *Trem2<sup>+/-</sup>* brain (Figures 3B–3D; FDR  $< 0.05$ ; interaction  $p < 0.01$  for 12 week CPZ, two-way ANOVA). Further comparison revealed that *Trem2<sup>-/-</sup>* brain significantly accumulated CE species containing polyunsaturated fatty acids, such as CE22:6 (docosahexaenoic acid) and CE20:4 (arachidonic acid) (Figure 3C; interaction  $p < 0.0001$ , two-way ANOVA).

CE22:6 showed the most striking increase in *Trem2<sup>-/-</sup>* brain with chronic demyelination, upward of 38-fold compared with *Trem2<sup>-/-</sup>* control brain and 2.5-fold compared with *Trem2<sup>+/+</sup>* 12 week CPZ brain (Figure 3C). Likewise, oxCE species, previously reported only in atherosclerotic lesions (Choi et al., 2017; Hutchins et al., 2011), were significantly enhanced in *Trem2<sup>-/-</sup>* brain compared with *Trem2<sup>+/+</sup>* with chronic demyelination, although they were found at much lower levels than CE (Figure 3D; interaction  $p < 0.01$  for 12 week CPZ, two-way ANOVA). Despite the significant accumulation of CE, brain cholesterol levels remained unaltered (Figure 3E). Other neutral lipids, such as triacylglycerol (TG), were elevated in *Trem2<sup>-/-</sup>* brain upon CPZ treatment (Figure 3F; interaction  $p < 0.05$ , two-way ANOVA). Ganglioside GM3d38:1 and d40:1 were also increased in *Trem2<sup>-/-</sup>* brain with chronic demyelination (Figure 3G; interaction  $p < 0.05$ , two-way ANOVA), reminiscent of lysosomal storage disorders. LCMS of mouse plasma did not reveal any genotype- or CPZ-specific differences in cholesterol and CE levels (Data S3; two-way ANOVA). These data indicate that chronic demyelination causes a profound alteration of cholesterol metabolism selectively in *Trem2<sup>-/-</sup>* CNS.

### TREM2 Deficiency Causes CE Accumulation in Isolated Microglia

The increase in CE found in *Trem2<sup>-/-</sup>* brain upon chronic demyelination may be primarily intracellular, resulting from phagocytosis of cholesterol-rich myelin by brain phagocytes and storage in lipid droplets after conversion of cholesterol to CE by ACAT. Alternatively, if *Trem2<sup>-/-</sup>* phagocytes are unable to properly engulf myelin debris, the latter may accumulate in the interstitial space and/or the cerebral spinal fluid (CSF), potentially generating CE extracellularly. To test this, we developed cell-type-specific lipidomics via isolation of microglia (CD11b<sup>+</sup>/CD45<sup>low</sup>) and astrocytes (ACSA2<sup>+</sup>) using FACS (Figure S4A) and collected CSF to assess circulating levels of lipids in the CNS.

As observed in forebrain, 12 week CPZ increased levels of certain lipid species in microglia of all genotypes compared with untreated genotype controls, but *Trem2<sup>-/-</sup>* microglia exhibited more dramatic increases compared with *Trem2<sup>+/+</sup>* and *Trem2<sup>+/-</sup>* microglia (Figure 4A; Data S3; two-way ANOVA, FDR  $< 0.05$ ). There were no genotype effects in microglia without CPZ. Lipid changes were unique to microglia, as astrocytes or CSF did not display any genotype- or CPZ treatment-specific alterations (Figures 4B and 4C; two-way ANOVA, FDR  $< 0.05$ ).

Lipids selectively increased in *Trem2<sup>-/-</sup>* microglia upon chronic demyelination included many species dysregulated in the forebrain (e.g., CE20:4, CE22:6) (Figures 4D and 4E; interaction  $p < 0.001$  for 12 week CPZ, two-way ANOVA), which were elevated 8- to 20-fold in *Trem2<sup>-/-</sup>* microglia upon 12 week CPZ diet compared with controls. Myelin-enriched lipids (Podbielska et al., 2011) or metabolites thereof, such as hexosylceramide (HexCer) d18:1/22:0, d18:1/24:0, and d18:1/24:1, galactosylceramide (GalCer) d18:1/22:0 and d18:1/24:0, ceramide (Cer) d18:1/24:1, and sulfatide d18:1/24:0, d18:1/24:0h, and d18:1/24:1, were significantly elevated upon 5 week CPZ treatment without genotype effects, suggesting comparable microglial uptake of myelin upon acute demyelination (treatment effect  $p < 0.05$  for 5 week CPZ, two-way ANOVA; Data S3). HexCer

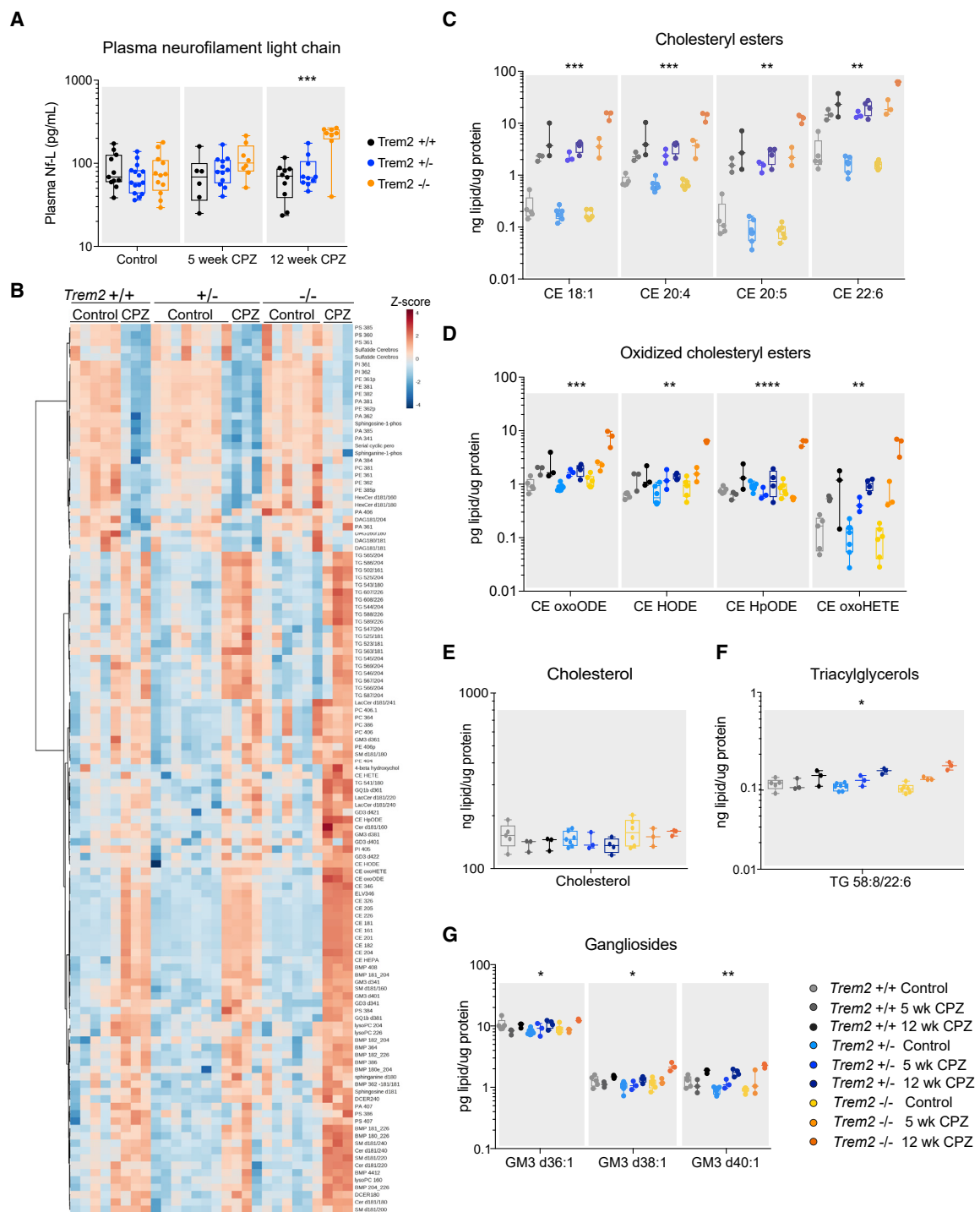


**Figure 3. TREM2 Deficiency Causes CE Accumulation in the Brain**

(A) Neurofilament light chain (NF-L) levels in plasma isolated from *Trem2*<sup>+/+</sup>, *Trem2*<sup>+/-</sup>, and *Trem2*<sup>-/-</sup> mice with control, 5 week, or 12 week CPZ diet. Genotype-treatment interaction with 12 week CPZ: \*\*\*p < 0.001, two-way ANOVA; n = 7–16 mice per condition. Data represent median ± max/min.

(B) Heatmap of lipids significantly altered by genotype and/or 12 week CPZ in mouse forebrain. Two-way ANOVA, FDR < 0.05; columns represent individual mice; n = 3–7 mice per condition.

(C-G) Concentration of (C) CE, (D) oxidized CE, (E) cholesterol, (F) triacylglycerol (TG), and (G) GM3 lipid species from mouse forebrain with control, 5 week, or 12 week CPZ diet. Data represent median  $\pm$  max/min. Two-way ANOVA fitted for 5 week and 12 week CPZ diet; genotype-treatment interaction with 12 week CPZ: \* $p$  < 0.05, \*\* $p$  < 0.01, and \*\*\* $p$  < 0.001. No significant genotype-treatment interaction with 5 week CPZ diet.

See also Figure S3 and Data S3.

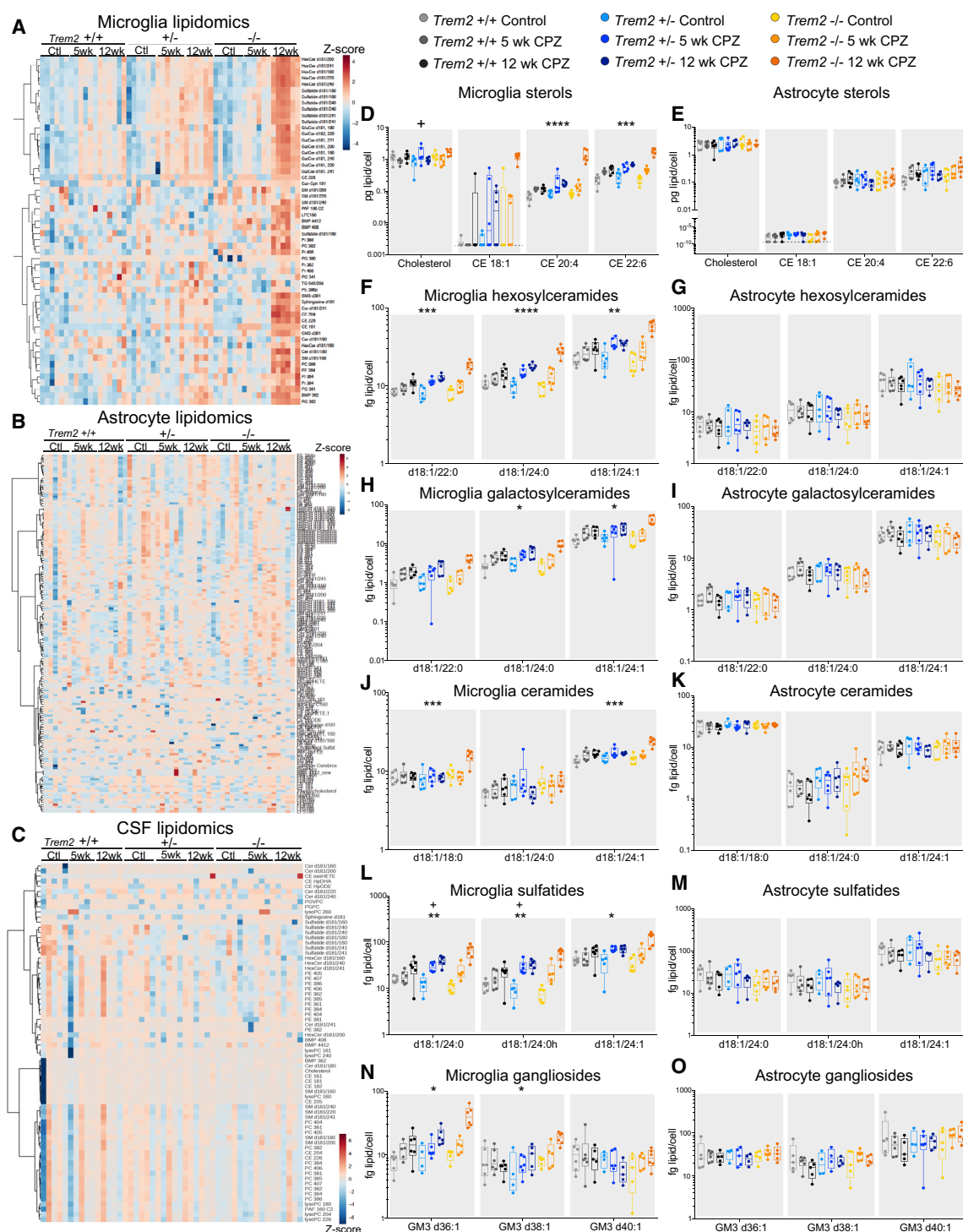


**Figure 4. TREM2 Deficiency Causes CE Accumulation in Isolated Microglia**

(A) Heatmap of lipids significantly altered by treatment and/or genotype in microglia isolated from *Trem2*<sup>+/+</sup>, *Trem2*<sup>+/-</sup>, and *Trem2*<sup>-/-</sup> mouse brain upon control, 5 week, or 12 week CPZ diet. Two-way ANOVA, FDR < 0.05; columns represent individual mice; n = 6 mice per condition.

(B and C) Heatmap comparison of lipids detected in (B) astrocytes or (C) cerebral spinal fluid (CSF) isolated from *Trem2* mice upon control, 5 week, or 12 week CPZ diet. Columns represent individual mice; n = 5 or 6 mice per condition.

(D–O) Concentrations of significantly altered lipid species in (A) from microglia or astrocytes isolated from mouse brain with control, 5 week, or 12 week CPZ diet: (D and E) sterols, including free cholesterol and CE, from (D) microglia or (E) astrocytes; (F and G) HexCer from (F) microglia or (G) astrocytes; (H and I) GalCer from

(legend continued on next page)

species, GalCer d18:1/24:0 and d18:1/24:1, Cer d18:1/18:0 and d18:1/24:1, and sulfatides were further enriched in *Trem2*<sup>-/-</sup> microglia compared with *Trem2*<sup>+/+</sup> upon 12 week CPZ (Figures 4F–4M; genotype-treatment interaction  $p < 0.05$ , two-way ANOVA). Additionally, GM3d36:1, GM3d38:1, and BMP36:2 were elevated in *Trem2*<sup>-/-</sup> microglia upon 12 week CPZ diet (Figures 4N, 4O, S4B, and S4C), potentially indicating lysosomal dysfunction (Bissig and Gruenberg, 2013; Miranda et al., 2018). LCMS analysis of CSF from the three genotypes with or without CPZ did not show any lipid changes (Figures S4D–S4H), suggesting that lipid accumulation observed in bulk forebrain tissue does not reflect extracellular accumulation, although changes in interstitial fluid cannot be ruled out. Thus, *Trem2*<sup>-/-</sup> microglia are able to phagocytose myelin debris during demyelination but are unable to properly metabolize or mediate the efflux of myelin lipids. Microglia sorted from the brain of aged *Trem2*<sup>+/+</sup> and *Trem2*<sup>-/-</sup> mice were also analyzed for lipid content, but no genotype-specific alteration of CE was found, consistent with minor alterations in cholesterol metabolism-related genes compared with CPZ-treated *Trem2*<sup>-/-</sup> microglia (Figures S1G and S1H).

### APOE Deficiency Results in a Broader CE Accumulation in the Brain

*Apoe* is one of the most striking TREM2-dependent damage-associated microglia genes (Götzl et al., 2019; Krasemann et al., 2017; Parhizkar et al., 2019) and is commonly believed to be the main cholesterol transporter in the CNS. Additionally, microglial responses in the *Apoe*<sup>-/-</sup> phenocopy those of *Trem2*<sup>-/-</sup> in specific paradigms, such as phagocytosis of apoptotic neurons (Krasemann et al., 2017). APOE deficiency may thus also produce microglial CE accumulation with CPZ, reflecting reduced CNS cholesterol transport. However, unlike TREM2, APOE is expressed in microglia and astrocytes, raising the possibility that APOE deficiency may more broadly affect brain cholesterol metabolism. We subjected *Apoe*<sup>+/+</sup> and *Apoe*<sup>-/-</sup> mice to a control or 12 week CPZ diet prior to LCMS analyses of forebrain, isolated microglia, astrocytes, and CSF. Lack of APOE generally increased brain CE levels (Figure 5A; Data S4). Levels of CE18:1 and CE22:6 were increased by 2.7- and 4-fold, respectively, in *Apoe*<sup>-/-</sup> forebrain relative to wild-type forebrain with control diet. CPZ led to an increase in CE18:1, 20:4, and 22:6 species in *Apoe*<sup>-/-</sup> versus *Apoe*<sup>+/+</sup> forebrain (Figure 5B; main effect from two-way ANOVA,  $p < 0.001$ ; FCs were 6.6, 1.4, and 6.7, respectively), and APOE deficiency significantly exacerbated the treatment effects for CE18:1 and CE20:4 (genotype-treatment interaction  $p < 0.05$ ). In addition, levels of BMP 40:8 and 44:12 were higher in the *Apoe*<sup>-/-</sup> forebrain, consistent with lysosomal defects (Figure S5A;  $p < 0.05$ ). There was a genotype-specific increase in all CE species in sorted microglia (Figures 5C and 5D; Data S4;  $p < 0.0001$ , two-way ANOVA), with 3.2-, 6.9-, and 2.5-fold increases in CE18:1, CE20:4, and CE22:6, respectively, in *Apoe*<sup>-/-</sup> microglia relative to wild-type microglia on control diet. With CPZ, changes were 2.8-, 4.2-,

and 2.3-fold, respectively, compared with wild-type microglia, suggesting that CPZ increases the levels of most CE species similarly in wild-type and *Apoe*<sup>-/-</sup> microglia, thus preserving genotype differences. Genotype-specific increases in CE were present in sorted astrocytes (Figures 5E and 5F; Data S4;  $p < 0.001$ , two-way ANOVA), with 2.1- and 4.5-fold increases in CE18:1 and CE22:6, respectively, in *Apoe*<sup>-/-</sup> astrocytes relative to wild-type astrocytes with CPZ. Interaction between genotype and CPZ was observed for CE18:1 ( $p < 0.05$ ). Remarkably, no changes were found for cholesterol in the forebrain or sorted glial cells (Figures 5B, 5D, and 5F). Myelin lipids HexCer and sulfatides were similarly increased in wild-type and *Apoe*<sup>-/-</sup> microglia with 12 week CPZ, but there were no treatment effects in astrocytes (Figures S5B and S5C; Data S4). Unlike in *Trem2*<sup>-/-</sup> CSF, CEs were elevated in *Apoe*<sup>-/-</sup> CSF, pointing to a widespread increase of these sterols in mutant brain (Figures S5D and S5E). Therefore, impaired cholesterol transport resulting from APOE deficiency causes massive, primarily CPZ-independent, accumulation of CE in forebrain, glial cells, and CSF. The fact that *Trem2*<sup>-/-</sup> microglia exhibit similar CE storage and have lower APOE levels suggests that the lipid phenotype stems from cholesterol transport defects.

### Myelin Sulfatide Binds TREM2 and Promotes Downstream Signaling

Next, we sought to delineate the mechanisms underlying lipid dysregulation in *Trem2*<sup>-/-</sup> cells *in vitro*. Myelin lipid accumulation in mutant cells could result from either increased phagocytosis or reduced lipid clearance post-phagocytosis. Because *Trem2*<sup>-/-</sup> myeloid cells generally show reduced phagocytosis (Kleinberger et al., 2014; Poliani et al., 2015), *Trem2*<sup>-/-</sup> microglia lipid phenotypes are unlikely to reflect increased myelin phagocytosis. Prior to investigating myelin phagocytosis in *Trem2*<sup>-/-</sup> cells, we assessed the ability of specific myelin lipids to bind and signal via TREM2, which may in turn regulate the phagocytic clearance of myelin.

TREM2 binds to various lipids, including phosphatidylcholine (PC), sphingomyelin (SM), phosphatidylserine (PS), phosphatidylinositol (PI), and sulfatide (Kober et al., 2016; Sudom et al., 2018; Wang et al., 2015), some of which (e.g., sulfatide) are myelin enriched (Du and Grabowski, 2004). We generated liposomes harboring candidate TREM2 ligands composed of 70 molar % PC with 30 molar % of a test lipid to assess TREM2 stimulation. Upon lipid ligand binding, TREM2 recruits SYK via DAP12's ITAM domain, leading to SYK phosphorylation (Hamerman et al., 2006). We stably overexpressed human DAP12 in the presence or absence of human TREM2 (hTREM2) in HEK293 cells (Figure S6A) and monitored phospho-SYK (pSYK) levels as a readout for receptor activation, using a TREM2 agonist antibody as a positive control. PS-, PI-, GalCer-, and sulfatide-containing liposomes increased pSYK levels in TREM2/DAP12 HEK293 cells (Figure 6A). To examine lipid signaling via endogenous TREM2, we differentiated human

(H) microglia or (I) astrocytes; (J and K) ceramides from (J) microglia or (K) astrocytes; (L and M) sulfatides from (L) microglia or (M) astrocytes; and (N and O) gangliosides from (N) microglia or (O) astrocytes. Data represent median  $\pm$  max/min. Two-way ANOVA fitted for 5 week and 12 week CPZ diet; genotype-treatment interaction with 5 (\* $p < 0.05$ ) or 12 week CPZ diet (\* $p < 0.05$ , \*\* $p < 0.01$ , and \*\*\* $p < 0.001$ ). Independent genotype or treatment effects noted in Data S3. See also Figure S4.

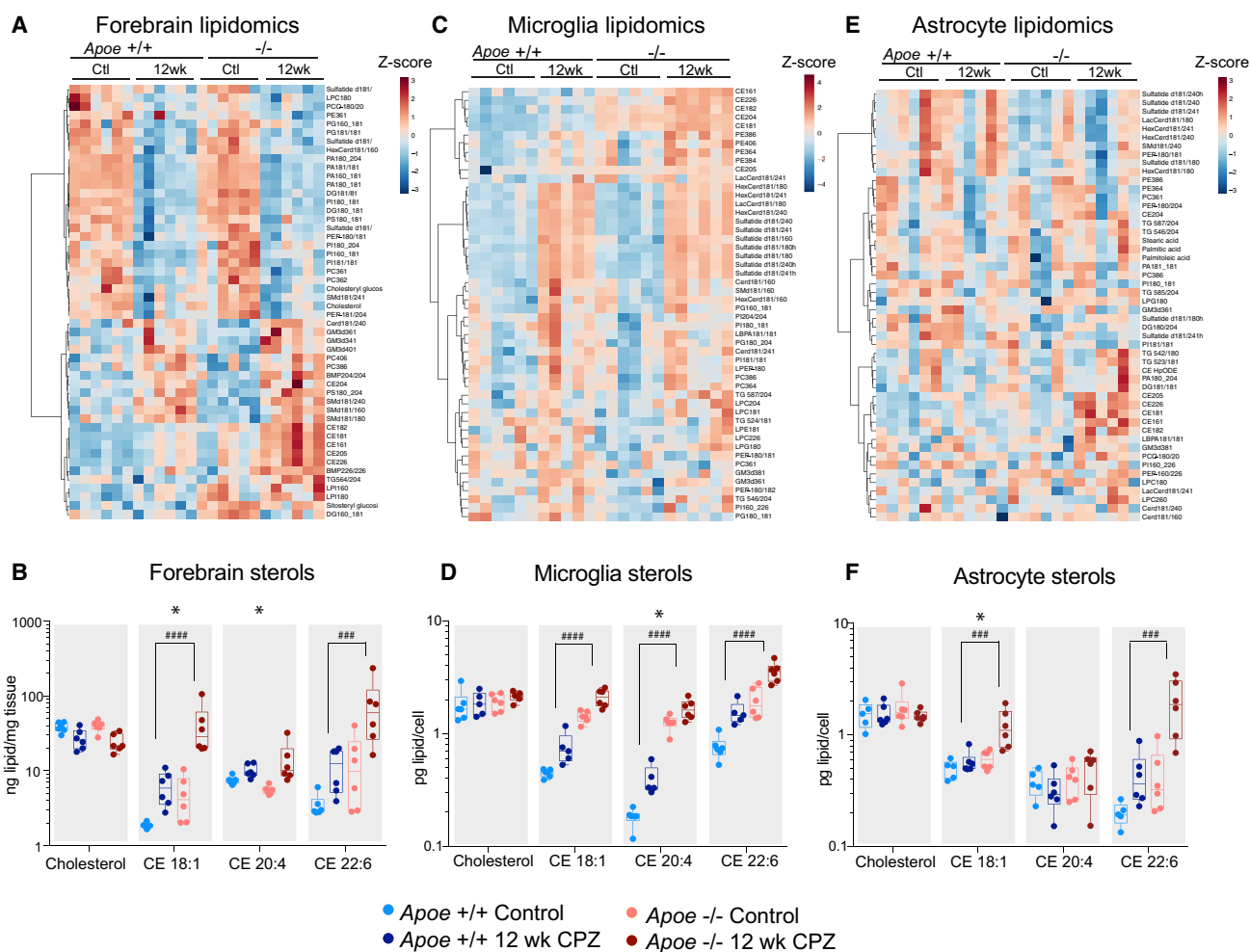


**Figure 5. APOE Deficiency Causes CE Accumulation in the Brain, Sorted Microglia, and Astrocytes**

(A) Heatmap of top 50 lipid species (ranked by ANOVA p value) altered by genotype and/or 12 week CPZ diet in *Apoe*<sup>+/+</sup> and *Apoe*<sup>-/-</sup> mouse forebrain.

(B) Concentration of free cholesterol and CE species from *Apoe*<sup>+/+</sup> and *Apoe*<sup>-/-</sup> mouse forebrain extracts with control or 12 week CPZ diet.

(C) Heatmap of top 50 lipid species (ranked by ANOVA p value) altered by genotype and/or 12 week CPZ diet in *Apoe*<sup>+/+</sup> and *Apoe*<sup>-/-</sup> sorted microglia.

(D) Concentration of free cholesterol and CE species from *Apoe*<sup>+/+</sup> and *Apoe*<sup>-/-</sup> sorted microglia with control or 12 week CPZ diet.

(E) Heatmap of top 50 lipid species (ranked by ANOVA p value) altered by genotype and/or 12 week CPZ diet in *Apoe*<sup>+/+</sup> and *Apoe*<sup>-/-</sup> sorted astrocytes.

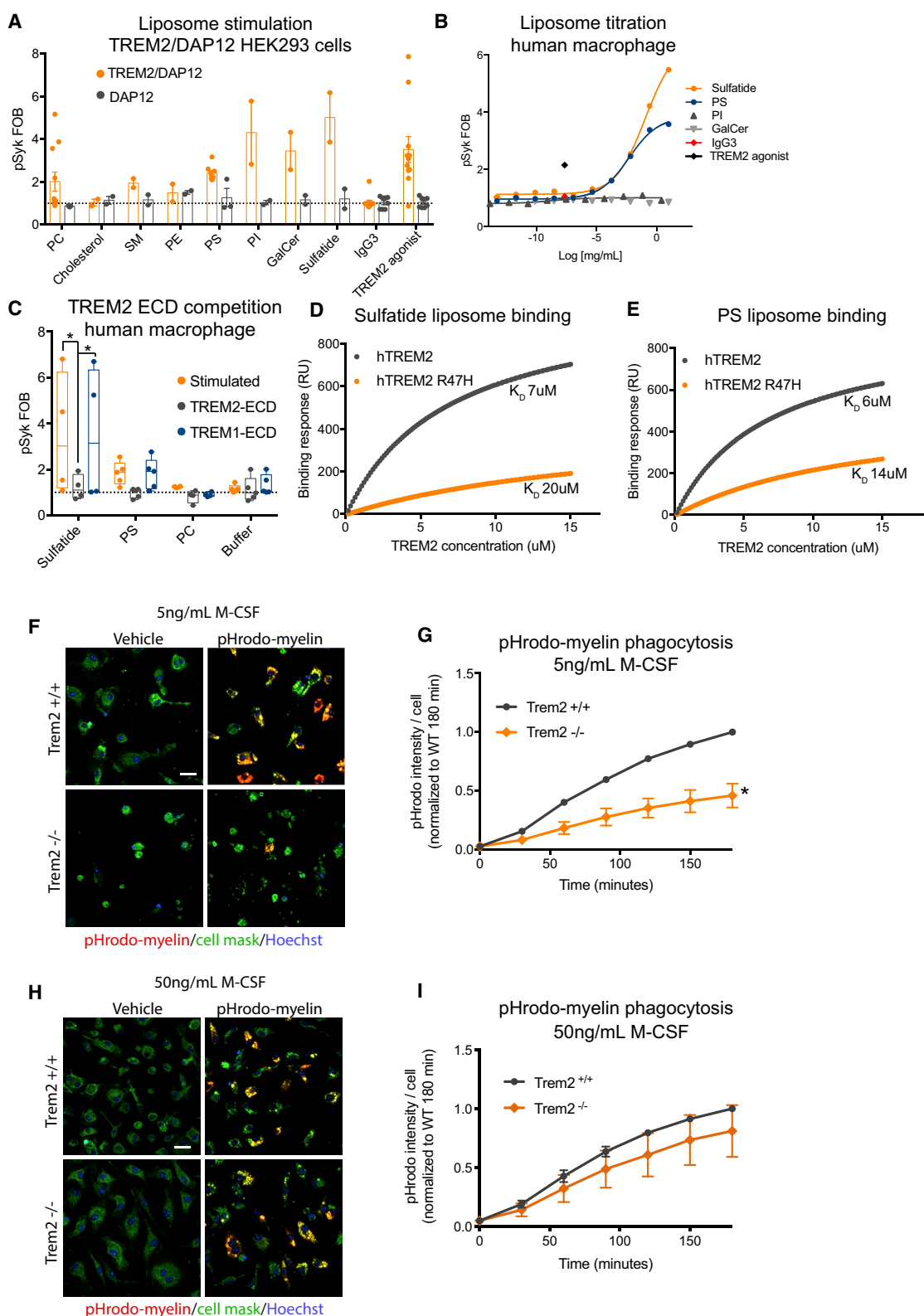
(F) Concentration of free cholesterol and CE species from *Apoe*<sup>+/+</sup> and *Apoe*<sup>-/-</sup> sorted astrocytes with control or 12 week CPZ diet.

In (B), (D), and (F), data represent median  $\pm$  max/min ( $n = 6$ ). Two-way ANOVA; genotype effects: \*\*\* $p < 0.001$  and \*\*\*\* $p < 0.0001$ ; genotype-treatment interactions: \* $p < 0.05$ . Treatment effects are noted in Data S4. See also Figure S5.

peripheral blood monocytes into macrophages (Figure S6B). Cells showed liposome dose-dependent increases in pSYK levels selectively for sulfatide and PS (Figure 6B). Increased pSYK response to sulfatide liposomes was abolished by addition of recombinant hTREM2 but not hTREM1 ECD, confirming TREM2 binding and signaling specificity (Figure 6C).

Certain *TREM2* LOAD variants, including R47H, show reduced affinity to lipids (Kober et al., 2016; Ulland and Colonna, 2018; Wang et al., 2015). We characterized the binding affinity and kinetics of sulfatide and PS to the ECD of wild-type and mutant TREM2 R47H (Figure S6C) with surface plasmon resonance. hTREM2 exhibited similar binding affinity and response at the highest analyte concentration to sulfatide- and PS-containing liposomes:  $K_D = 6.8 \mu\text{M}$ , response units

(RU) = 704, and  $K_D = 5.6 \mu\text{M}$ , RU = 631, respectively (Figures 6D and 6E). In comparison, hTREM2 R47H showed reduced affinity and lower binding response (i.e., RU) for sulfatide and PS liposomes:  $K_D = 20 \mu\text{M}$ , RU = 191, and  $K_D = 14 \mu\text{M}$ , RU = 267, respectively, suggesting ligand specificity (Figures 6D and 6E). Lower binding response was due to a faster off-rate of the interaction, leading to shorter residency of mutant TREM2 on the lipid surface. Decreased affinity and response values observed with the R47H variant were accounted for by 5-fold (sulfatide) and 2.4-fold (PS) faster off-rates and relatively similar on-rates (Figures S6D–S6G). These data show that sulfatide binds and signals via TREM2 and that the R47H LOAD variant is significantly impaired in its interaction with this lipid.



(legend on next page)

## High M-CSF Rescues Myelin Phagocytosis Defects in *Trem2*<sup>-/-</sup> BMDMs

Because TREM2 binds to myelin lipids such as sulfatide, *Trem2*<sup>-/-</sup> cells may be impaired in myelin uptake, although our *in vivo* CPZ data suggest that myelin lipid uptake is unchanged in *Trem2*<sup>-/-</sup> microglia. To evaluate acute myelin uptake *in vitro*, we treated *Trem2*<sup>+/+</sup> and *Trem2*<sup>-/-</sup> BMDMs with pHrodo-conjugated myelin, after verifying loss of TREM2 protein in null cells (Figures S6H and S6I). At low concentrations of pro-survival factor M-CSF (5 ng/mL), pHrodo-myelin phagocytosis was reduced in *Trem2*<sup>-/-</sup> BMDMs compared with *Trem2*<sup>+/+</sup>, consistent with previous studies (Poliani et al., 2015) (Figures 6F and 6G). However, at high concentrations of M-CSF (50 ng/mL), pHrodo-myelin phagocytosis was comparable for both genotypes (Figures 6H and 6I). Thus, high levels of M-CSF may provide compensatory upregulation of phagocytic pathways in *Trem2*<sup>-/-</sup> BMDMs and reveal that the phagocytosis defects in TREM2-deficient cells can be context dependent. Importantly, although they are obtained from BMDMs, these data do not support a mechanism by which increased myelin binding or phagocytosis causes lipid accumulation in *Trem2*<sup>-/-</sup> microglia *in vivo*, prompting further mechanistic analyses.

## CE Accumulation in *Trem2*<sup>-/-</sup> Cells Is Rescued by ACAT1 Inhibitor and LXR Agonist *In Vitro*

Because *Trem2*<sup>-/-</sup> BMDMs can normally phagocytose myelin in high M-CSF, we tested if accumulation of neutral lipids, including CE, occurs downstream of myelin phagocytosis in null cells. BMDMs were treated with 25 µg/mL myelin over 48 h, then stained with Nile red to assess neutral lipid storage with fluorescence microscopy. *Trem2*<sup>-/-</sup> BMDMs exhibited neutral lipid accumulation upon myelin treatment, as shown by an ~3-fold increase in Nile red stain (Figures 7A and 7B). Lipidomics also revealed prominent genotype-specific accumulation of CE18:2, CE20:4, and CE20:5 (Figure 7C; Data S5; p < 0.01, two-way ANOVA). Cholesterol and various species of TG, diacylglycerol (DG), and myelin-derived HexCer also accumulated in *Trem2*<sup>-/-</sup> BMDMs (Figure 7C). These changes were reminiscent of those observed in *Trem2*<sup>-/-</sup> microglia *in vivo* with CPZ diet (Figure 4).

Next, we tested if CE accumulation in *Trem2*<sup>-/-</sup> BMDMs is due to excess storage of myelin cholesterol by ACAT1, which converts free cholesterol to CE in the endoplasmic reticulum. Because myelin debris contain high levels of cholesterol but low levels of CE, CE can accumulate in lipid droplets only if myelin-derived cholesterol escapes from lysosomes post-phagocytosis. BMDMs were treated for 48 h with myelin and co-dosed with ACAT1 inhibitor (500 nM K604) (Ikenoya et al., 2007). LCMS analysis showed that K604 selectively rescues the accumulation of most CE species in response to myelin in both genotypes, suggesting myelin cholesterol is indeed stored as an esterified form in lipid droplets (Figure 7C; Data S5).

We subsequently asked if CE accumulation in *Trem2*<sup>-/-</sup> BMDMs is specific to myelin phagocytosis or if other physiologically relevant uptake mechanisms, such as endocytosis of CE-containing lipoproteins, may cause a similar CE increase. First, we tested if oxidized low-density lipoprotein (oxLDL) binds and stimulates TREM2, using low-density lipoprotein (LDL) as a control. Using our hTREM2/hDAP12 HEK293 line, we found that oxLDL elevates pSYK levels (Figure S7A). A dose-dependent increase in pSYK levels was found in oxLDL-treated human macrophages (Figure S7B). The increase trended toward attenuation by pre-incubating oxLDL with high concentrations of recombinant hTREM2 ECD at 9 µM (p = 0.1, two-way ANOVA, Tukey test) but not at lower concentrations such as those used in liposome/hTREM2 competition experiments (3 µM) (Figures S7C and S7D), consistent with the fact that oxLDL is known to bind and stimulate multiple immune receptors (Choi et al., 2017). When treated chronically with 50 µg/mL oxLDL, *Trem2*<sup>-/-</sup> BMDM exhibited an increase in Nile red stain (Figures S7D and S7E), which did not stem from increased oxLDL uptake by *Trem2*<sup>-/-</sup> BMDMs, as indicated by comparable internalization of Dil-labeled oxLDL (Figure S7F). By LCMS, certain species of CE, TG, HexCer, and cholesterol displayed genotype-specific increases in both vehicle and oxLDL-treated conditions (Figure S7G; Data S5). K604 reduced levels of CE20:5 and CE22:6 in *Trem2*<sup>-/-</sup> BMDMs upon oxLDL exposure (Figure S7G; p < 0.05, Student's t test), albeit less substantially than seen in

**Figure 6. Myelin Sulfatide Binds TREM2 and Promotes Downstream Signaling**

- (A) Phospho-SYK (pSYK) fold change in TREM2/DAP12-HEK293 cells stimulated with indicated liposomes, normalized to buffer control (dotted line) and compared with TREM2 agonist antibody and isotype control. N ≥ 2 experimental replicates from two or more averaged technical replicates. PE, phosphatidylethanolamine. Data represent mean ± SEM.
- (B) Liposome titration curve of pSYK fold changes in human macrophage cells from two to four donors upon stimulation with indicated test lipid, normalized to buffer control, and compared with TREM2 antibody and isotype control.
- (C) Liposome stimulation of indicated test lipid in human macrophage cells from four or five donors with liposomes only (stimulated) or liposomes with 3 µM recombinant TREM2- or TREM1-extracellular domain (ECD) protein normalized to buffer control (dotted line). \*p < 0.05, two-way ANOVA, Tukey test. Data represent median ± min/max.
- (D) Surface plasmon resonance binding response of increasing concentrations of wild-type (gray) and mutant R47H (orange) hTREM2 protein to (D) 30% sulfatide/70%PC or (E) 30% PS/70% PC 100 nm liposomes.
- (F) *Trem2*<sup>+/+</sup> and *Trem2*<sup>-/-</sup> BMDM vehicle or pHrodo-myelin (red) phagocytosis with 5 ng/mL M-CSF. Green, cell membrane stain; blue, Hoechst. Scale bar: 20 µm.
- (G) Intensity of pHrodo-myelin (5 µg/mL) phagocytosis in *Trem2*<sup>+/+</sup> and *Trem2*<sup>-/-</sup> BMDMs with 5 ng/mL M-CSF. Data represent mean ± SEM (n = 3 biological replicates); \*p < 0.05 comparing *Trem2*<sup>+/+</sup> and *Trem2*<sup>-/-</sup> AUC, two-tailed t test.
- (H) *Trem2*<sup>+/+</sup> and *Trem2*<sup>-/-</sup> BMDM vehicle or pHrodo-myelin (red) phagocytosis with 50 ng/mL M-CSF. Green, cell membrane stain; blue, Hoechst. Scale bar: 20 µm.
- (I) Intensity of pHrodo-myelin (5 µg/mL) phagocytosis in *Trem2*<sup>+/+</sup> and *Trem2*<sup>-/-</sup> BMDM with 50 ng/mL M-CSF. Data represent mean ± SEM (n = 3 biological replicates).

See also Figure S6.

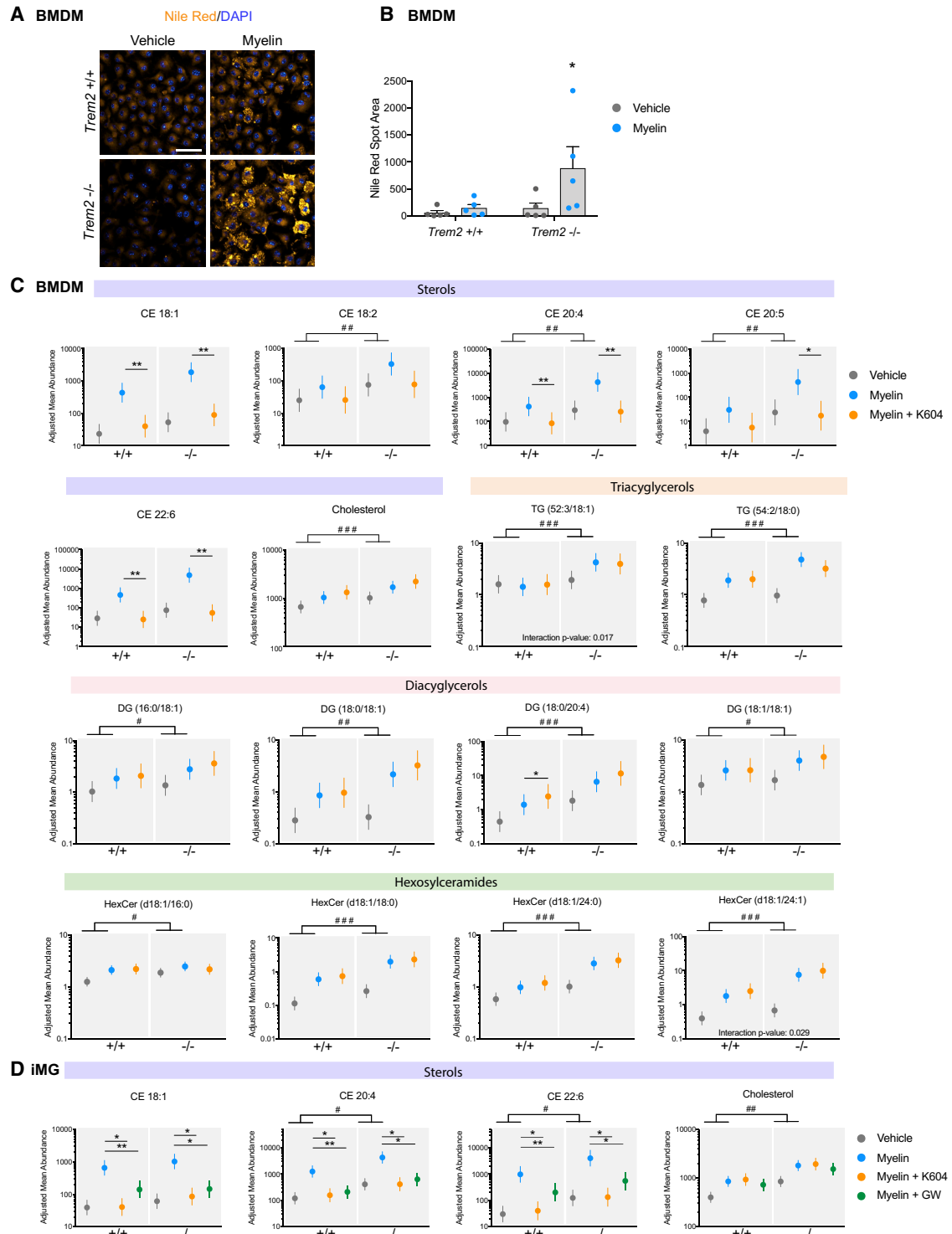


**Figure 7. TREM2 Deficiency-Associated CE Accumulation Is Rescued by ACAT1 Inhibitor and LXR Agonist In Vitro**

(A) Nile red stain of neutral lipids in BMDMs cultured from Trem2<sup>+/+</sup> and Trem2<sup>-/-</sup> mice, treated with vehicle or 25 µg/mL purified myelin for 48 h. Scale bar: 50 µm.

(B) Quantification of total spot area of Nile red stain in vehicle or 25 µg/mL myelin-treated Trem2<sup>+/+</sup> and Trem2<sup>-/-</sup> BMDMs. Data represent mean + SEM (n = 5 biological replicates); \*p < 0.05; one-tailed t test for comparison between Trem2<sup>+/+</sup> with myelin versus Trem2<sup>-/-</sup> with myelin.

(C and D) Quantification of Trem2<sup>+/+</sup> and Trem2<sup>-/-</sup> (C) sterols, TG, diacylglycerols (DG), and HexCer from cultured BMDMs and (D) sterols from cultured iPSC-derived microglia (iMG) treated with vehicle, myelin, or myelin with ACAT1 inhibitor K604 (500 nM) or LXR agonist GW3965 (10 µM) for 48 h. Batch-adjusted mean

(legend continued on next page)

myelin uptake experiments (Figure 7C), without altering cholesterol or other lipid levels (Figure S7G; Data S5). In contrast to the myelin uptake paradigm, ACAT1 is responsible for only a fraction of CE accumulation in oxLDL-treated *Trem2<sup>-/-</sup>* BMDMs, suggesting that a pool of CE accumulates in organelles other than lipid droplets, likely lysosomes.

Next, we sought a relevant *in vitro* model to extend our findings to human cells. We differentiated human iPSCs into microglia and established that the transcriptome is similar to that of primary human microglia (Figure S7H). We then genetically ablated TREM2 using CRISPR (Figure S7I) and found that *TREM2<sup>-/-</sup>* iPSC-derived microglia (iMG) have a ~20% decrease in pHrodo-myelin uptake relative to wild-type iMG after a 4 h incubation ( $n = 4$  technical replicates). Despite reduced myelin phagocytosis, there was a genotype-specific increase in CE20:4, CE22:6, and cholesterol (Figure 7D; Data S5; CE,  $p < 0.05$ ; cholesterol,  $p < 0.01$  [two-way ANOVA]). As in BMDMs, the increase in CE, but not cholesterol, was abolished by the ACAT1 inhibitor (Figure 7D;  $p < 0.05$ , Student's t test).

Drugs such as LXR agonists can reduce CE stores by upregulating the expression of ABCA1 and ABCG1 transporters (Moore and Tabas, 2011). We thus treated iMG with the LXR agonist GW3695 which enhanced the mRNA expression of *ABCA1* (by  $10.3 \pm 0.2$  and  $14.8 \pm 2.1$  fold in wild-type and knockout iMG, respectively) and *ABCG1* (by  $46.6 \pm 5.0$  and  $53.8 \pm 2.9$  fold in wild-type and knockout iMG, respectively;  $n = 2$  biological replicates). GW3695 rescued CE accumulation in myelin-treated *TREM2<sup>+/+</sup>* and *TREM2<sup>-/-</sup>* iMG (Figure 7D; Data S5; *TREM2<sup>+/+</sup>* iMG,  $p < 0.01$ ; *TREM2<sup>-/-</sup>* iMG,  $p < 0.05$  [Student's t test]). Our data suggest that TREM2 deficiency causes cholesterol efflux defects, leading to accumulation of an ACAT1 inhibitor-sensitive pool of CE in human iMG.

## DISCUSSION

Growing evidence indicates that TREM2 signaling is necessary for normal microglial functions, including control of proliferation, survival, energy metabolism, and gene expression (Deczkowska et al., 2018; Ulland and Colonna, 2018; Yeh et al., 2017). Although a link has been established between TREM2 and lipid metabolism, previous studies have focused primarily on lipids as candidate TREM2 ligands, in the form of either lipoprotein particles or cell surface-exposed signals (Atagi et al., 2015; Bailey et al., 2015; Sudom et al., 2018; Ulland and Colonna, 2018; Wang et al., 2016; Yeh et al., 2016). Further clues that TREM2 mediates microglial lipid metabolism stemmed from microarray studies (Poliani et al., 2015). Recently, TREM2 was shown to control blood cholesterol metabolism in obese mice by modulating the macrophage transcriptome in adipose tissue, further linking TREM2 to lipid metabolism (Jaitin et al., 2019). Here, we combined FACS-based CNS cell type isolation with RNA-seq, scRNA-seq, and lipidomics to establish a key role of TREM2 signaling in the control of microglial cholesterol transport

and metabolism. TREM2 LOF caused robust intracellular accumulation of a storage form of cholesterol, CE, which is also observed in glial cells lacking APOE, the main cholesterol transporter in the CNS. This function of TREM2 was revealed by a chronic CPZ challenge that exposed microglia to myelin debris, which are enriched for cholesterol and signaling lipids, such as sulfatides. Lipid ligands are recognized by the TREM2 ECD and mediate downstream signaling, which we hypothesize may enable resolution of disease pathology within the damaged CNS parenchyma.

As shown by scRNA-seq analysis of sorted microglia, CPZ leads to TREM2-dependent gene expression changes in a subset of microglia as part of a transition to DAM-like states related to those found in other disease models (Keren-Shaul et al., 2017). This transcriptional program encompasses a gene “toolbox” that may enable microglia to enhance not only their chemotactic and phagocytic properties but also their lysosomal degradative capacity and ability to facilitate intracellular and extracellular cholesterol transport, including efflux from microglia. Failure to induce this transcriptional program in *Trem2<sup>-/-</sup>* microglia results in lipid accumulation rather than phagocytic defects per se, suggesting that impaired lipid metabolism may represent a critical aspect of TREM2 LOF in chronic diseases, including Nasu-Hakola disease and LOAD. This maladaptive state leads to neuritic dystrophy and Nf-L release, a phenomenon generally reflective of neurodegeneration (Blennow and Zetterberg, 2018). Whether LOAD-associated LOF *TREM2* variants (e.g., R47H) phenocopy the complete LOF remains to be established.

*Trem2<sup>-/-</sup>* macrophages and microglia exhibit a severe CE storage disorder reminiscent of macrophage foam cells in atherosclerotic lesions (Moore and Tabas, 2011). Cholesterol dyshomeostasis in foam cells is generally associated with pro-inflammatory responses (Choi et al., 2017; Heneka et al., 2018; Moore and Tabas, 2011). Familial cases of atherosclerosis linked to mutations in the *LIPA* gene (encoding the lysosomal acid lipase) lead to a CE storage disorder, suggesting that accumulation of this lipid is pathogenic, at least in lysosomes (Du and Grabowski, 2004). CE accumulation may mediate toxicity via enzymatic or non-enzymatic generation of oxidized metabolites and lipid peroxidation products from the mono- or polyunsaturated fatty acyl chains it harbors (Choi et al., 2017; Hutchins et al., 2011). Most of the brain cholesterol is found in myelin, and thus excessive release of myelin debris in disease situations may cause cholesterol- or CE-induced toxicity, because cholesterol cannot be efficiently catabolized and is deleterious to cells at high concentrations. Our *in vivo* studies indicate that the cholesterol burden imposed upon microglia by chronic demyelination leads to severe CE storage in *Trem2<sup>-/-</sup>* microglia, which likely reflects impairment in the metabolic flux of cholesterol in these cells. By failing to upregulate multiple genes involved in cholesterol transport (*Apoe*, *Apoc1*, *Npc2*) and metabolism (*Lipa*, *Nceh1*, *Ch25h*) upon chronic phagocytic challenge,

and 95% confidence interval for each group,  $n = 3$  biological replicates. Significant genotype effect (two-way ANOVA, comparing vehicle and myelin treatments in *Trem2<sup>+/+</sup>* and *Trem2<sup>-/-</sup>* cells):  $\#p < 0.05$ ,  $\#\#p < 0.01$ , and  $\#\#\#p < 0.001$ . Significant drug treatment effects within each genotype (Student's t test):  $*p < 0.05$  and  $**p < 0.01$ .

See also Figure S7 and Data S5.

*Trem2*<sup>-/-</sup> cells accumulate intracellular CE to the detriment of microglial function. Reduced metabolic flux of CE may expose it to oxidation, resulting in secondary accumulation of oxCE species, as observed in *Trem2*<sup>-/-</sup> mouse brain. Whether oxCE species are neurotoxic or contribute to inflammation as seen in atherosclerotic lesions remains to be determined (Choi et al., 2017).

Our *in vitro* studies showed that post-phagocytic conversion of myelin-derived cholesterol to CE by ACAT1, followed by its storage in lipid droplets, underlies the molecular basis for CE accumulation in *Trem2*<sup>-/-</sup> cells. Further mechanistic dissection indicated that TREM2<sup>-/-</sup> iMG are defective in cholesterol efflux, on the basis of the ability of an LXR agonist to fully alleviate CE accumulation. Because TREM2 regulates microglial expression of APOE, an apolipoprotein that can function both in lipid intake and lipid efflux (Shi and Holtzman, 2018; Tall, 2008), a likely mechanism accounting for CE accumulation in *Trem2*<sup>-/-</sup> cells is reduced efflux of cholesterol onto APOE-containing lipoproteins. This is consistent with our *Apoe*<sup>-/-</sup> CPZ studies, showing CE accumulation in mutant brain, sorted astrocytes, and microglia. *Trem2*<sup>-/-</sup> and *Apoe*<sup>-/-</sup> mice thus share phenotypic similarities, although APOE, unlike TREM2, is expressed in astrocytes and thus controls CNS cholesterol metabolism more broadly. APOE isoform-specific differences in the handling of lipids by glial cells may also account for the lower and higher genetic risk of *APOE2* and *APOE4* (relative to *APOE3*) to LOAD, respectively. The fact that human iPSC-derived *APOE4/E4* astrocytes were recently reported to accumulate endolysosomal cholesterol suggests that cholesterol metabolism in glial cells could be implicated in LOAD (Lin et al., 2018). As several other LOAD genes expressed in microglia mediate lipid metabolism (e.g., *CLU*, *ABCA7*, *SORL1*), alteration of cholesterol and CE metabolism in microglia may be a unifying mechanism accounting for disease risk, perhaps via impacts on A $\beta$ , tau, inflammation, or other AD-relevant pathogenic processes.

The initial characterization of AD pathology by Dr. Alzheimer noted accumulation of “adipose inclusions,” likely neutral lipids, in glial cells from postmortem brain samples of patients with dementia (Foley, 2010). More recent studies have indicated the relevance of CE in AD, as it accumulates in postmortem brain tissue from patients and in the brain of *PSEN1/APP* mutant mice (Astarita et al., 2011; Chan et al., 2012; Morel et al., 2013) and other neurodegenerative models (Miranda et al., 2018). Importantly, genetic ablation and pharmacological inhibition of ACAT1, which lowers CE levels, is protective in amyloid and tauopathy models through various mechanisms, including autophagy activation (Bhattacharya and Kovacs, 2010; Bryleva et al., 2010; Di Paolo and Kim, 2011; Hutter-Paier et al., 2004; Puglielli et al., 2001; Shibuya et al., 2015). However, with the exception of Shibuya et al. (2014), these studies primarily examined the role of ACAT1 in neurons and did not test if ACAT1 inhibitors decrease CE burden in microglia. Brain-penetrant LXR agonists have also been considered as therapeutics on the basis of anti-inflammatory and amyloid-lowering properties, resulting from their ability to enhance cholesterol efflux. However, they may present safety liabilities from broad impact on all cell types and peripheral lipid metabolism (Moutinho and Landreth, 2017). Our study raises the possibility that enhancing TREM2 function may selectively alleviate cholesterol and CE burden in myeloid cells, including microglia, potentially providing therapeutic

benefits in LOAD and other diseases associated with lipid dysregulation.

## STAR★METHODS

Detailed methods are provided in the online version of this paper and include the following:

- KEY RESOURCES TABLE
- LEAD CONTACT AND MATERIALS AVAILABILITY
- EXPERIMENTAL MODEL AND SUBJECT DETAILS
  - Animals
  - Cell Lines
  - Primary Cell Cultures
- METHOD DETAILS
  - Immunofluorescence
  - Neurofilament light detection
  - Fluorescence activated cell sorting (FACS)
  - RNA isolation, qPCR, QuantSeq library preparation, and analysis
  - Single cell RNAseq library preparation
  - Single cell RNAseq data processing
  - Single cell RNAseq cluster and expression analysis
  - Brain sample collection and preparation for LCMS analysis
  - FACS lipid extraction
  - CSF sample collection and preparation for LCMS analysis
  - LCMS analysis of lipids
  - Liposome preparation
  - pSYK AlphaLISA
  - Recombinant purification of His tagged hTREM2 and hTREM2 R47H ECD
  - Lipid binding analysis using surface plasmon resonance (SPR)
  - Myelin purification and phagocytosis
  - Lipid challenge experiments in BMDMs and human iPSC-derived microglia
- QUANTIFICATION AND STATISTICAL ANALYSIS
- DATA AND CODE AVAILABILITY

## SUPPLEMENTAL INFORMATION

Supplemental Information can be found online at <https://doi.org/10.1016/j.neuron.2019.12.007>.

## ACKNOWLEDGMENTS

We thank Rishi Rahkit and Nathan Moerke for help developing the pSYK assay and Connie Ha for help with RNA-seq. We thank Kimberly Scearce-Levie, Zachary Sweeney, Nga Bien-Ly, and Jeff Kessler for critical reading of the manuscript. This study was funded by Denali Therapeutics.

## AUTHOR CONTRIBUTIONS

K.M.M. and G.D.P. conceived the study. A.A.N., K.L., B.V.L., S.L., D.J.K., D.X., H.C., P.C.G.H., P.E.S., T.S., G.A., J.W.L., K.M.M., and G.D.P. designed experiments. A.A.N., K.L., B.V.L., J.W., L.P., S.S.D., C.L., D.J.K., D.X., A.L., S.B., T.K.E., P.C.G.H., M.L., J.S., B.J.A., T.L., H.O.S., A.S., and G.A. performed experiments. T.S. performed the QuantSeq analyses. S.L. performed the scRNA-seq analyses. A.A.N., K.L., B.V.L., S.L., J.W., L.P., S.S.D., D.J.K., J.C.D.,

B.J.A., T.S., and G.A. analyzed data. L.P., T.L., J.W.L., P.E.S., S.B.P., and R.J.W. edited the manuscript. A.A.N., K.L., B.V.L., S.L., T.S., G.A., K.M.M., and G.D.P. wrote the manuscript.

#### DECLARATION OF INTERESTS

All authors are paid employees and shareholders of Denali Therapeutics. R.J.W. is a founder and member of the Board of Directors of Denali. Denali has filed patent applications related to the subject matter of this paper.

Received: December 24, 2018

Revised: August 7, 2019

Accepted: December 4, 2019

Published: January 2, 2020

#### REFERENCES

- Astarita, G., Jung, K.M., Vasilevko, V., Dipatrizio, N.V., Martin, S.K., Cribbs, D.H., Head, E., Cotman, C.W., and Piomelli, D. (2011). Elevated stearoyl-CoA desaturase in brains of patients with Alzheimer's disease. *PLoS ONE* 6, e24777.
- Atagi, Y., Liu, C.C., Painter, M.M., Chen, X.F., Verbeeck, C., Zheng, H., Li, X., Rademakers, R., Kang, S.S., Xu, H., et al. (2015). Apolipoprotein E is a ligand for triggering receptor expressed on myeloid cells 2 (TREM2). *J. Biol. Chem.* 290, 26043–26050.
- Bailey, C.C., DeVaux, L.B., and Farzan, M. (2015). The triggering receptor expressed on myeloid cells 2 binds apolipoprotein E. *J. Biol. Chem.* 290, 26033–26042.
- Bemiller, S.M., McCray, T.J., Allan, K., Formica, S.V., Xu, G., Wilson, G., Kokiko-Cochran, O.N., Crish, S.D., Lasagna-Reeves, C.A., Ransohoff, R.M., et al. (2017). TREM2 deficiency exacerbates tau pathology through dysregulated kinase signaling in a mouse model of tauopathy. *Mol. Neurodegener* 12, 74.
- Benjamini, Y., and Hochberg, Y. (1995). Controlling the false discovery rate: a practical and powerful approach to multiple testing. *J. R. Stat. Soc. Ser. A Stat. Soc.* 57, 289–300.
- Bhattacharyya, R., and Kovacs, D.M. (2010). ACAT inhibition and amyloid beta reduction. *Biochim. Biophys. Acta* 1801, 960–965.
- Bissig, C., and Gruenberg, J. (2013). Lipid sorting and multivesicular endosome biogenesis. *Cold Spring Harb. Perspect. Biol.* 5, a016816.
- Blennow, K., and Zetterberg, H. (2018). Biomarkers for Alzheimer's disease: current status and prospects for the future. *J. Intern. Med.* 284, 643–663.
- Blondel, V.D., Guillaume, J.L., Lambiotte, R., and Lefebvre, E. (2008). Fast unfolding of communities in large networks. *J. Stat. Mech.* 2008, P1008.
- Bryleva, E.Y., Rogers, M.A., Chang, C.C., Buen, F., Harris, B.T., Rousselet, E., Seidah, N.G., Oddo, S., LaFerla, F.M., Spencer, T.A., et al. (2010). ACAT1 gene ablation increases 24(S)-hydroxycholesterol content in the brain and ameliorates amyloid pathology in mice with AD. *Proc. Natl. Acad. Sci. U S A* 107, 3081–3086.
- Cantoni, C., Bollman, B., Licastro, D., Xie, M., Mikesell, R., Schmidt, R., Yuede, C.M., Galimberti, D., Olivecrona, G., Klein, R.S., et al. (2015). TREM2 regulates microglial cell activation in response to demyelination in vivo. *Acta Neuropathol.* 129, 429–447.
- Carmona, S., Hardy, J., and Guerreiro, R. (2018). The genetic landscape of Alzheimer disease. *Handb. Clin. Neurol.* 148, 395–408.
- Chan, R.B., Oliveira, T.G., Cortes, E.P., Honig, L.S., Duff, K.E., Small, S.A., Wenk, M.R., Shui, G., and Di Paolo, G. (2012). Comparative lipidomic analysis of mouse and human brain with Alzheimer disease. *J. Biol. Chem.* 287, 2678–2688.
- Choi, S.H., Sviridov, D., and Miller, Y.I. (2017). Oxidized cholesteryl esters and inflammation. *Biochim. Biophys. Acta Mol. Cell. Biol. Lipids* 1862, 393–397.
- Chong, J., Soufan, O., Li, C., Caraus, I., Li, S., Bourque, G., Wishart, D.S., and Xia, J. (2018). MetaboAnalyst 4.0: towards more transparent and integrative metabolomics analysis. *Nucl. Acids. Res.* 46, 486–494.
- Deczkowska, A., Amit, I., and Schwartz, M. (2018). Microglial immune checkpoint mechanisms. *Nat. Neurosci.* 21, 779–786.
- Di Paolo, G., and Kim, T.W. (2011). Linking lipids to Alzheimer's disease: cholesterol and beyond. *Nat. Rev. Neurosci.* 12, 284–296.
- Dobin, A., Davis, C.A., Schlesinger, F., Drenkow, J., Zaleski, C., Jha, S., Batut, P., Chaisson, M., and Gingeras, T.R. (2013). STAR: ultrafast universal RNA-seq aligner. *Bioinformatics* 29, 15–21.
- Doench, J.G., Fusi, N., Sullender, M., Hegde, M., Vainberg, E.W., Donovan, K.F., Smith, I., Tothova, Z., Wilen, C., Orchard, R., et al. (2016). Optimized sgRNA design to maximize activity and minimize off-target effects of CRISPR-Cas9. *Nat. Biotechnol.* 34, 184–191.
- Du, H., and Grabowski, G.A. (2004). Lysosomal acid lipase and atherosclerosis. *Curr. Opin. Lipidol.* 15, 539–544.
- Durinck, S., Moreau, Y., Kasprzyk, A., Davis, S., De Moor, B., Brazma, A., and Huber, W. (2005). BioMart and Bioconductor: a powerful link between biological databases and microarray data analysis. *Bioinformatics* 21, 3439–3440.
- Efthymiou, A.G., and Goate, A.M. (2017). Late onset Alzheimer's disease genetics implicates microglial pathways in disease risk. *Mol. Neurodegener.* 12, 43.
- Fabregat, A., Jupe, S., Matthews, L., Sidiropoulos, K., Gillespie, M., Garapati, P., Haw, R., Jassal, B., Korninger, F., May, B., et al. (2018). The Reactome Pathway Knowledgebase. *Nucleic Acids Res.* 46 (D1), D649–D655.
- Foley, P. (2010). Lipids in Alzheimer's disease: A century-old story. *Biochimica et Biophysica Acta* 1801, 750–753.
- Götzl, J.K., Brendel, M., Werner, G., Parhizkar, S., Sebastian Monasor, L., Kleinberger, G., Colombo, A.V., Deussing, M., Wagner, M., Winkelmann, J., et al. (2019). Opposite microglial activation stages upon loss of PGRN or TREM2 result in reduced cerebral glucose metabolism. *EMBO Mol. Med.* 11, e9711.
- Guerreiro, R., Wojtas, A., Bras, J., Carrasquillo, M., Rogeava, E., Majounie, E., Cruchaga, C., Sassi, C., Kauwe, J.S., Younkin, S., et al.; Alzheimer Genetic Analysis Group (2013). TREM2 variants in Alzheimer's disease. *N. Engl. J. Med.* 368, 117–127.
- Hamerman, J.A., Jarjoura, J.R., Humphrey, M.B., Nakamura, M.C., Seaman, W.E., and Lanier, L.L. (2006). Cutting edge: inhibition of TLR and FcR responses in macrophages by triggering receptor expressed on myeloid cells (TREM)-2 and DAP12. *J. Immunol.* 177, 2051–2055.
- Hammond, T.R., Robinton, D., and Stevens, B. (2018). Microglia and the brain: complementary partners in development and disease. *Annu. Rev. Cell Dev. Biol.* 34, 523–544.
- Heneka, M.T., McManus, R.M., and Latz, E. (2018). Inflammasome signalling in brain function and neurodegenerative disease. *Nat. Rev. Neurosci.* 19, 610–621.
- Hutchins, P.M., Moore, E.E., and Murphy, R.C. (2011). Electrospray MS/MS reveals extensive and nonspecific oxidation of cholesterol esters in human peripheral vascular lesions. *J. Lipid Res.* 52, 2070–2083.
- Hutter-Paier, B., Huttunen, H.J., Puglielli, L., Eckman, C.B., Kim, D.Y., Hofmeister, A., Moir, R.D., Domnitz, S.B., Frosch, M.P., Windisch, M., and Kovacs, D.M. (2004). The ACAT inhibitor CP-113,818 markedly reduces amyloid pathology in a mouse model of Alzheimer's disease. *Neuron* 44, 227–238.
- Ikenoya, M., Yoshinaka, Y., Kobayashi, H., Kawamine, K., Shibuya, K., Sato, F., Sawanobori, K., Watanabe, T., and Miyazaki, A. (2007). A selective ACAT-1 inhibitor, K-604, suppresses fatty streak lesions in fat-fed hamsters without affecting plasma cholesterol levels. *Atherosclerosis* 191, 290–297.
- Ilicic, T., Kim, J.K., Kolodziejczyk, A.A., Bagger, F.O., McCarthy, D.J., Marioni, J.C., and Teichmann, S.A. (2016). Classification of low quality cells from single-cell RNA-seq data. *Genome Biol.* 17, 29.
- Jaitin, D.A., Adlung, L., Thaiss, C.A., Weiner, A., Li, B., Descamps, H., Lundgren, P., Bleriot, C., Liu, Z., Deczkowska, A., et al. (2019). Lipid-associated macrophages control metabolic homeostasis in a Trem2-dependent manner. *Cell* 178, 686–698.e14.
- Jay, T.R., Hirsch, A.M., Broihier, M.L., Miller, C.M., Neilson, L.E., Ransohoff, R.M., Lamb, B.T., and Landreth, G.E. (2017). Disease progression-dependent

- effects of TREM2 deficiency in a mouse model of Alzheimer's disease. *J. Neurosci.* 37, 637–647.
- Jiang, H., Lei, R., Ding, S.W., and Zhu, S. (2014). Skewer: a fast and accurate adapter trimmer for next-generation sequencing paired-end reads. *BMC Bioinformatics* 15, 182.
- Jonsson, T., Stefansson, H., Steinberg, S., Jónsdóttir, I., Jonsson, P.V., Snaedal, J., Björnsson, S., Huttenlocher, J., Levey, A.I., Lah, J.J., et al. (2013). Variant of TREM2 associated with the risk of Alzheimer's disease. *N. Engl. J. Med.* 368, 107–116.
- Keren-Shaul, H., Spinrad, A., Weiner, A., Matcovitch-Natan, O., Dvir-Szternfeld, R., Ulland, T.K., David, E., Baruch, K., Lara-Astaiso, D., Toth, B., et al. (2017). A unique microglia type associated with restricting development of Alzheimer's disease. *Cell* 169, 1276–1290.e17.
- Kleinberger, G., Yamanishi, Y., Suárez-Calvet, M., Czirr, E., Lohmann, E., Cuyvers, E., Struyf, H., Pettkus, N., Wenninger-Weinzierl, A., Mazaheri, F., et al. (2014). TREM2 mutations implicated in neurodegeneration impair cell surface transport and phagocytosis. *Sci. Transl. Med.* 6, 243ra86.
- Kober, D.L., Alexander-Brett, J.M., Karch, C.M., Cruchaga, C., Colonna, M., Holtzman, M.J., and Brett, T.J. (2016). Neurodegenerative disease mutations in TREM2 reveal a functional surface and distinct loss-of-function mechanisms. *eLife* 5, e20391.
- Krasemann, S., Madore, C., Cialic, R., Baufeld, C., Calcagno, N., El Fatimy, R., Beckers, L., O'Loughlin, E., Xu, Y., Fanek, Z., et al. (2017). The TREM2-APOE pathway drives the transcriptional phenotype of dysfunctional microglia in neurodegenerative diseases. *Immunity* 47, 566–581.e9.
- Kucukural, A., Yukselen, O., Ozata, D.M., Moore, M.J., and Garber, M. (2019). DEBrowser: interactive differential expression analysis and visualization tool for count data. *BMC Genomics* 20, 6.
- Lee, C.Y.D., Daggett, A., Gu, X., Jiang, L.L., Langfelder, P., Li, X., Wang, N., Zhao, Y., Park, C.S., Cooper, Y., et al. (2018). Elevated TREM2 gene dosage reprograms microglia responsiveness and ameliorates pathological phenotypes in Alzheimer's disease models. *Neuron* 97, 1032–1048.e5.
- Leyns, C.E.G., Gratuze, M., Narasimhan, S., Jain, N., Koscal, L.J., Jiang, H., Manis, M., Colonna, M., Lee, V.M.Y., Ulrich, J.D., and Holtzman, D.M. (2019). TREM2 function impedes tau seeding in neuritic plaques. *Nat. Neurosci.* 22, 1217–1222.
- Leyns, C.E.G., Ulrich, J.D., Finn, M.B., Stewart, F.R., Koscal, L.J., Serrano, J.R., Robinson, G.O., Anderson, E., Colonna, M., and Holtzman, D.M. (2017). TREM2 deficiency attenuates neuroinflammation and protects against neurodegeneration in a mouse model of tauopathy. *PNAS* 114, 11524–11529.
- Liao, Y., Smyth, G.K., and Shi, W. (2014). featureCounts: an efficient general purpose program for assigning sequence reads to genomic features. *Bioinformatics* 30, 923–930.
- Lin, Y.T., Seo, J., Gao, F., Feldman, H.M., Wen, H.L., Penney, J., Cam, H.P., Gjoneska, E., Raja, W.K., Cheng, J., et al. (2018). APOE4 causes widespread molecular and cellular alterations associated with Alzheimer's disease phenotypes in human iPSC-derived brain cell types. *Neuron* 98, 1141–1154.e7.
- Liu, L., Zhang, K., Sandoval, H., Yamamoto, S., Jaiswal, M., Sanz, E., Li, Z., Hui, J., Graham, B.H., Quintana, A., and Bellen, H.J. (2015). Glial lipid droplets and ROS induced by mitochondrial defects promote neurodegeneration. *Cell* 160, 177–190.
- Lun, A.T., Bach, K., and Marioni, J.C. (2016a). Pooling across cells to normalize single-cell RNA sequencing data with many zero counts. *Genome Biol.* 17, 75.
- Lun, A.T., McCarthy, D.J., and Marioni, J.C. (2016b). A step-by-step workflow for low-level analysis of single-cell RNA-seq data with Bioconductor. *F1000Res.* 5, 2122.
- Martin, M.G., Pfrieger, F., and Dotti, C.G. (2014). Cholesterol in brain disease: sometimes determinant and frequently implicated. *EMBO Rep.* 15, 1036–1052.
- Masuda, T., Sankowski, R., Staszewski, O., Böttcher, C., Amann, L., Sagar, Scheiwe, C., Nessler, S., Kunz, P., van Loo, G., et al. (2019). Author correction: spatial and temporal heterogeneity of mouse and human microglia at single-cell resolution. *Nature* 568, E4.
- McCarthy, D.J., Campbell, K.R., Lun, A.T., and Wills, Q.F. (2017). Scater: pre-processing, quality control, normalization and visualization of single-cell RNA-seq data in R. *Bioinformatics* 33, 1179–1186.
- Mecca, C., Giambanco, I., Donato, R., and Arcuri, C. (2018). Microglia and aging: the role of the TREM2-DAP12 and CX3CL1-CX3CR1 axes. *Int. J. Mol. Sci.* 19, E318.
- Miranda, A.M., Lasiecka, Z.M., Xu, Y., Neufeld, J., Shahriar, S., Simoes, S., Chan, R.B., Oliveira, T.G., Small, S.A., and Di Paolo, G. (2018). Neuronal lysosomal dysfunction releases exosomes harboring APP C-terminal fragments and unique lipid signatures. *Nat. Commun.* 9, 291.
- Moore, K.J., and Tabas, I. (2011). Macrophages in the pathogenesis of atherosclerosis. *Cell* 145, 341–355.
- Morel, E., Chamoun, Z., Lasiecka, Z.M., Chan, R.B., Williamson, R.L., Vetanovetz, C., Dall'Armi, C., Simoes, S., Point Du Jour, K.S., McCabe, B.D., et al. (2013). Phosphatidylinositol-3-phosphate regulates sorting and processing of amyloid precursor protein through the endosomal system. *Nat. Commun.* 4, 2250.
- Moutinho, M., and Landreth, G.E. (2017). Therapeutic potential of nuclear receptor agonists in Alzheimer's disease. *J. Lipid Res.* 58, 1937–1949.
- Muffat, J., Li, Y., Yuan, B., Mitalipova, M., Omer, A., Corcoran, S., Bakiasi, G., Tsai, L.H., Aubourg, P., Ransohoff, R.M., and Jaenisch, R. (2016). Efficient derivation of microglia-like cells from human pluripotent stem cells. *Nat. Med.* 22, 1358–1367.
- Paloneva, J., Manninen, T., Christman, G., Hovanes, K., Mandelin, J., Adolfsson, R., Bianchin, M., Bird, T., Miranda, R., Salmaggi, A., et al. (2002). Mutations in two genes encoding different subunits of a receptor signaling complex result in an identical disease phenotype. *Am. J. Hum. Genet.* 71, 656–662.
- Pandya, H., Shen, M.J., Ichikawa, D.M., Sedlock, A.B., Choi, Y., Johnson, K.R., Kim, G., Brown, M.A., Elkahloun, A.G., Maric, D., et al. (2017). Differentiation of human and murine induced pluripotent stem cells to microglia-like cells. *Nat. Neurosci.* 20, 753–759.
- Parhizkar, S., Arzberger, T., Brendel, M., Kleinberger, G., Deussing, M., Focke, C., Nuscher, B., Xiong, M., Ghasemigharagoz, A., Katzmarski, N., et al. (2019). Loss of TREM2 function increases amyloid seeding but reduces plaque-associated ApoE. *Nat. Neurosci.* 22, 191–204.
- Podbielska, M., Levery, S.B., and Hogan, E.L. (2011). The structural and functional role of myelin fast-migrating cerebrosides: pathological importance in multiple sclerosis. *Clin. Lipidol.* 6, 159–179.
- Poliani, P.L., Wang, Y., Fontana, E., Robinette, M.L., Yamanishi, Y., Gilfillan, S., and Colonna, M. (2015). TREM2 sustains microglial expansion during aging and response to demyelination. *J. Clin. Invest.* 125, 2161–2170.
- Praet, J., Guglielmetti, C., Berneman, Z., Van der Linden, A., and Ponsaerts, P. (2014). Cellular and molecular neuropathology of the cuprizone mouse model: clinical relevance for multiple sclerosis. *Neurosci. Biobehav. Rev.* 47, 485–505.
- Puglielli, L., Konopka, G., Pack-Chung, E., Ingano, L.A., Berezovska, O., Hyman, B.T., Chang, T.Y., Tanzi, R.E., and Kovacs, D.M. (2001). Acyl-coenzyme A: cholesterol acyltransferase modulates the generation of the amyloid beta-peptide. *Nat. Cell Biol.* 3, 905–912.
- Ransohoff, R.M. (2016). How neuroinflammation contributes to neurodegeneration. *Science* 353, 777–783.
- Robinson, M.D., and Oshlack, A. (2010). A scaling normalization method for differential expression analysis of RNA-seq data. *Genome Biol.* 11, R25.
- Safaiyan, S., Kannaiyan, N., Snaidero, N., Brioschi, S., Biber, K., Yona, S., Edinger, A.L., Jung, S., Rossner, M.J., and Simons, M. (2016). Age-related myelin degradation burdens the clearance function of microglia during aging. *Nat. Neurosci.* 19, 995–998.
- Sala Frigerio, C., Wolfs, L., Fattorelli, N., Thrupp, N., Voytyuk, I., Schmidt, I., Mancuso, R., Chen, W.T., Woodbury, M.E., Srivastava, G., et al. (2019). The major risk factors for Alzheimer's disease: age, sex, and genes modulate the microglia response to Abeta plaques. *Cell Rep.* 27, 1293–1306.e6.
- Sayed, F.A., Telpoukhovskaia, M., Kodama, L., Li, Y., Zhou, Y., Le, D., Hauduc, A., Ludwig, C., Gao, F., Clelland, C., et al. (2018). Differential effects of partial

- and complete loss of TREM2 on microglial injury response and tauopathy. *PNAS* **115**, 10172–10177.
- Shi, Y., and Holtzman, D.M. (2018). Interplay between innate immunity and Alzheimer disease: APOE and TREM2 in the spotlight. *Nat. Rev. Immunol.* **18**, 759–772.
- Shibuya, Y., Chang, C.C., Huang, L.H., Bryleva, E.Y., and Chang, T.Y. (2014). Inhibiting ACAT1/SOAT1 in microglia stimulates autophagy-mediated lysosomal proteolysis and increases A $\beta$ 1-42 clearance. *J. Neurosci.* **34**, 14484–14501.
- Shibuya, Y., Chang, C.C., and Chang, T.Y. (2015). ACAT1/SOAT1 as a therapeutic target for Alzheimer's disease. *Future Med. Chem.* **7**, 2451–2467.
- Simes, R.J. (1986). An improved Bonferroni procedure for multiple tests of significance. *Biometrika* **73**, 751–754.
- Sudom, A., Talreja, S., Danao, J., Bragg, E., Kegel, R., Min, X., Richardson, J., Zhang, Z., Sharkov, N., Marcora, E., et al. (2018). Molecular basis for the loss-of-function effects of the Alzheimer's disease-associated R47H variant of the immune receptor TREM2. *J. Biol. Chem.* **293**, 12634–12646.
- Tall, A.R. (2008). Cholesterol efflux pathways and other potential mechanisms involved in the athero-protective effect of high density lipoproteins. *J. Intern. Med.* **263**, 256–273.
- Ulland, T.K., and Colonna, M. (2018). TREM2—a key player in microglial biology and Alzheimer disease. *Nat. Rev. Neurol.* **14**, 667–675.
- Ulland, T.K., Song, W.M., Huang, S.C., Ulrich, J.D., Sergushichev, A., Beatty, W.L., Loboda, A.A., Zhou, Y., Cairns, N.J., Kambal, A., et al. (2017). TREM2 maintains microglial metabolic fitness in Alzheimer's disease. *Cell* **170**, 649–663.e13.
- Wang, Y., Cella, M., Mallinson, K., Ulrich, J.D., Young, K.L., Robinette, M.L., Gilfillan, S., Krishnan, G.M., Sudhakar, S., Zinselmeyer, B.H., et al. (2015). TREM2 lipid sensing sustains the microglial response in an Alzheimer's disease model. *Cell* **160**, 1061–1071.
- Wang, Y., Ulland, T.K., Ulrich, J.D., Song, W., Tzaferis, J.A., Hole, J.T., Yuan, P., Mahan, T.E., Shi, Y., Gilfillan, S., et al. (2016). TREM2-mediated early microglial response limits diffusion and toxicity of amyloid plaques. *J. Exp. Med.* **213**, 667–675.
- Wickham, H. (2016). *ggplot2: elegant graphics for data analysis* (New York: Springer).
- Wu, D., and Smyth, G.K. (2012). Camera: a competitive gene set test accounting for inter-gene correlation. *Nucleic Acids Res.* **40**, e133.
- Xu, C., and Su, Z. (2015). Identification of cell types from single-cell transcriptomes using a novel clustering method. *Bioinformatics* **31**, 1974–1980.
- Yeh, F.L., Wang, Y., Tom, I., Gonzalez, L.C., and Sheng, M. (2016). TREM2 binds to apolipoproteins, including APOE and CLU/APOJ, and thereby facilitates uptake of amyloid-beta by microglia. *Neuron* **91**, 328–340.
- Yeh, F.L., Hansen, D.V., and Sheng, M. (2017). TREM2, microglia, and neurodegenerative diseases. *Trends Mol. Med.* **23**, 512–533.
- Yuan, P., Condello, C., Keene, C.D., Wang, Y., Bird, T.D., Paul, S.M., Luo, W., Colonna, M., Baddeley, D., and Grutzendler, J. (2016). TREM2 haploinsufficiency in mice and humans impairs the microglia barrier function leading to decreased amyloid compaction and severe axonal dystrophy. *Neuron* **90**, 724–739.

## STAR★METHODS

### KEY RESOURCES TABLE

REAGENT or RESOURCE	SOURCE	IDENTIFIER
<b>Antibodies</b>		
Rabbit anti-beta-APP	Life Technologies	512700; RRID: AB_87659
Mouse anti-SMI-32	Millipore	559844; RRID: AB_10682557
Rabbit anti-human PU.1	Cell Signaling Technology	2258; RRID: AB_2186909
Goat anti-human TREM2	R&D Systems	AF1828; RRID: AB_2208689
Alexa Fluor 555 goat anti-mouse	Life Technologies	A21422; RRID: AB_141822
Alexa Fluor 647 goat anti-mouse IgG1	Life Technologies	A21240; RRID: AB_141658
Alexa Fluor 546 goat anti-rabbit	Life Technologies	A11035; RRID: AB_143051
Alexa Fluor Plus 647 goat anti-rabbit	Thermo Fisher Scientific	A32733; RRID: AB_2633282
Alexa Fluor 488 donkey anti-sheep	Life Technologies	A11015; RRID: AB_141362
Mouse anti-NeuN	Millipore	MAB377; RRID: AB_2298772
CD11b-BV421	BD Biosciences	562605; RRID: AB_11152949
CD45-APC	BD Biosciences	559864; RRID: AB_398672
ACSA-2-PE	Miltenyi Biotec	130-102-365; RRID: AB_2651189
APC-conjugated rat-anti-human/mouse-TREM2	R&D Systems	MAB17291; RRID: AB_2208679
Sheep anti-Trem2	R&D Systems	AF1729; RRID: AB_354956
mouse anti-beta-Actin	Sigma	A2228; RRID: AB_476697
Mouse anti-Trem2	Abnova	MAB2056; RRID: AB_1716445
<b>Chemicals, Peptides, and Recombinant Proteins</b>		
ACAT inhibitor K604	This paper	Patent US 2004/0038987 A1
LXR agonist GW3965	Sigma	G6295
TREM1-His	Novoprotein Scientific	CS67
hTREM2-ECD	This paper	N/A
hTREM2-R47H-ECD	This paper	N/A
Murine M-CSF	Life Technologies	PMC2044
1,2-dioleoyl-sn-glycero-3-phosphocholine (DOPC)	Avanti Polar Lipids	850375C
Sulfatide	Avanti Polar Lipids	131305P
Phosphatidylserine	Avanti Polar Lipids	840039C
Sphingomyelin	Avanti Polar Lipids	860062C
Phosphatidylinositol	Avanti Polar Lipids	850144P
Galactosylceramide	Avanti Polar Lipids	860521P
Phosphatidylethanolamine	Echelon Biosciences	L-2118
Free cholesterol	Echelon Biosciences	L-6012
<b>Critical Commercial Assays</b>		
Adult brain dissociation kit	Miltenyi Biotec	130-107-677
RNeasy Plus Micro Kit	QIAGEN	74034
QuantSeq 3' mRNAseq Library Prep Kit	Lexogen	015.96
FWD for Illumina		
NEBNext Library Quant Kit for Illumina	New England Biolabs	E7630S
Chromium Single Cell 3' Library Kit with v2 chemistry	10X Genomics	120267
pSyk AlphaLISA assay	PerkinElmer	ALSU-PSYK-A10K
Simoa NF-light Advantage Kit	Quanterix	103186
pHrodo Red Microscale Labeling Kit	ThermoFisher	P35363

(Continued on next page)

**Continued**

REAGENT or RESOURCE	SOURCE	IDENTIFIER
<b>Deposited Data</b>		
Raw and processed RNA-sequencing data	This paper	GEO: GSE130627
Reactome Database	Fabregat et al., 2018	<a href="https://doi.org/10.18129/B9.bioc.reactome.db">https://doi.org/10.18129/B9.bioc.reactome.db</a>
<b>Experimental Models: Cell Lines</b>		
HEK293	ATCC	CRL-1573
Expi293F	ThermoFisher	A14527
Human iPSC	ThermoFisher	A18945
<b>Experimental Models: Organisms/Strains</b>		
Mouse: C57BL/6J- <i>Trem2</i> <sup>erm2Adju</sup> /J	The Jackson Laboratory	JAX: 027197
Mouse: B6.129P2- <i>Apoe</i> <sup>tm1Unc</sup> /J	The Jackson Laboratory	JAX: 002052
<b>Oligonucleotides</b>		
Trem2 sgRNA: TATGACTCCATGAAGCACTG	Integrated DNA Technologies	N/A
Trem2 murine Taqman probe	ThermoFisher	Mm04209422_m1
Cx3cr1 murine Taqman probe	ThermoFisher	Mm02620111_s1
Gfap murine Taqman probe	ThermoFisher	Mm01253033_m1
P2ry12 murine Taqman probe	ThermoFisher	Mm01950543_s1
Gapdh murine Taqman probe	ThermoFisher	Mm99999915_g1
<b>Recombinant DNA</b>		
pBudCE4.1-hTREM2_hDAP12	This paper	N/A
pBudCE4.1-hDAP12	This paper	N/A
pRK5-hTREM2	This paper	N/A
pRK5-hTREM2-R47H	This paper	N/A
<b>Software and Algorithms</b>		
R	<a href="https://www.R-project.org">https://www.R-project.org</a>	Version 3.5 (2018)
Prism	GraphPad	Versions 7-8
Harmony	PerkinElmer	HCA
Zen	Zeiss	Version 2.3
FastQC	<a href="http://www.bioinformatics.babraham.ac.uk/projects/fastqc">www.bioinformatics.babraham.ac.uk/projects/fastqc</a>	Version 0.11.5
Cell Ranger	10X Genomics	Version 2.1
MultiQuant	Sciex	Version 3.02
TargetLynx	Waters	Version 4.2
Analyst	Sciex	Version 1.6
Biacore T200 Evaluation Software	GE Healthcare	Version 3.1
MetaboAnalyst	<a href="https://www.metaboanalyst.ca">https://www.metaboanalyst.ca</a>	Version 4.0
<b>Other</b>		
Control mouse diet	Envigo	TD.160766
0.2% Cuprizone mouse diet	Envigo	TD.160765
Fixable Viability Stain BV510	BD Biosciences	564406
CellMask Deep Red Plasma Membrane Stain	ThermoFisher	C10046

**LEAD CONTACT AND MATERIALS AVAILABILITY**

- Further information and requests for resources and reagents should be directed to the Lead Contact, Gilbert Di Paolo ([dipaolo@dnli.com](mailto:dipaolo@dnli.com)).
- There are restrictions to the availability of TREM2/DAP12 HEK293 cells, DAP12 HEK293 cells, *TREM2*<sup>-/-</sup> iPSCs, pBudCE4.1-hTREM2\_hDAP12, pBudCE4.1-hDAP12, pRK5-hTREM2, pRK5-hTREM2-R47H, and K604. We will consider distribution under an MTA subject to restrictions from commercial source.

## EXPERIMENTAL MODEL AND SUBJECT DETAILS

### Animals

*Trem2<sup>-/-</sup>* mice were purchased from the Jackson Laboratory (Stock #: 027197) and backcrossed to C57BL/6J mice to generate *Trem2<sup>+/+</sup>* mice. *Trem2<sup>+/+</sup>* mice were further intercrossed to generate three genotypes of littermates (*Trem2<sup>+/+</sup>*, *Trem2<sup>+/-</sup>* and *Trem2<sup>-/-</sup>*) for this study.

Additional wild-type C57BL/6J mice from the same strain as littermate *Trem2<sup>+/+</sup>* mice were purchased (Jackson Laboratory) and acclimated to the in-house colony for 1-3 weeks prior to diet administration (n = 1-2 *Trem2<sup>+/+</sup>* and n = 1-5 C57BL/6J wild-type mice pooled for cohorts). Biochemical results did not differ between littermate controls and C57BL/6J mice. For CPZ groups, male and female mice 9-11 months of age were used. Each genotype of mice was divided into three groups with either a normal diet (Envigo TD.160766) or a cuprizone diet (0.2% cuprizone, Envigo TD.160765) treatment paradigm for 5 or 12 weeks (n = 3-6 mice/group for forebrain lipidomics and histology; n = 6 mice/group for FACS and CSF lipidomics; male and female mice were used in both cohorts, 1-3 females and 1-5 males per group). The body weight of each animal was recorded weekly to monitor the effects of cuprizone. For the APOE study, male and female *Apoe<sup>-/-</sup>* (Stock #: 2052) and wild-type C57BL/6J mice were purchased from Jackson Laboratory. Mice were 3 months of age at the start of either a normal diet or a 0.2% cuprizone diet for 12 weeks (n = 3 female and n = 3 male mice/group for forebrain, sorted glial cell, and CSF lipidomics). For the aging study, female *Trem2<sup>+/+</sup>* and *Trem2<sup>-/-</sup>* mice were used at 2 and 15-17 months of age (n = 7 mice/group) for young and aged groups, respectively. For all studies, littermate mice were group-housed whenever possible and littermates of the same gender were randomly assigned to experimental groups. No procedures were performed on mice prior to outlined studies. All mouse husbandry and experimental procedures were approved by Denali Institutional Animal Care and Use Committee.

### Cell Lines

#### **TREM2/DAP12 and DAP12 HEK293 stable cell lines**

HEK293 cells were transfected with a pBudCE4.1 Mammalian Expression Vector (Thermo-Fisher) expressing wild-type human TREM2 and DAP12, and DAP12 alone. Stable expressing clones were selected and the cell surface TREM2 expression was evaluated by flow cytometry with APC-conjugated rat anti-human/mouse-TREM2 monoclonal (R&D MAB17291). The highest wild-type TREM2 expressing clone was selected for expansion. The clones stably expressing DAP12 were analyzed by western blot. Cells were grown at 37°C, 5% CO<sub>2</sub> in T-150 flasks in DMEM containing 1X glutamax, 10% FBS, 1X Pen/Strep solution, and 200 µg/mL zeocin.

#### **Recombinant Expression of His tagged hTREM2 and hTREM2 R47H ECD**

The ecto domain (residues 19-172) of TREM2 was sub cloned in the pRK5 vector with the secretion signal from mouse Ig kappa chain V-III, amino acids 1-20 at the N-terminal region and a 6X-His tag at the C-terminal region. Expi293F cells were grown at 37°C, 5% CO<sub>2</sub>, 145rpm in Expi293 Expression Medium (ThermoFisher) and transfected using the Expi293 Expression System Kit according to the manufacturer's instructions.

#### **iPSC maintenance and genome editing**

iPSCs were obtained from ThermoFisher (#A18945) and maintained on Geltrex (Thermo #A1413302)-coated plates with mTeSR1 media (StemCell Technologies #85850) according to manufacturer's instructions. Knockout lines were generated using a nucleofection-based RNP approach to introduce Cas9 (NEB # M0646M) and sgRNAs against gene targets (crRNAs ordered from IDT) were introduced into iPSCs via nucleofection (Lonza P3 kit # V4XP-3032). sgRNAs were designed using the Broad Institute design tool based on a previous study (Doench et al., 2016). Clones were screened by T7 endonuclease and positive clones were further screened by TOPO cloning (Thermo cat #450030) to identify precise mutations.

#### **Differentiation of iPSCs to microglia**

iPSCs were first differentiated into hematopoietic progenitor cells following manufacturer's instructions using a commercially available kit (StemCell Technologies #05310). HPCs positive for identity markers CD34, CD43, and CD45 were transferred to a plate containing primary human astrocytes and co-cultured using media adapted from a previous study (Pandya et al., 2017). Once floating cells in co-culture are predominantly (> 80%) mature microglia, the microglia are transferred into homeostatic culture conditions adapted from previous work from others (Muffat et al., 2016) for 3-7 days prior to assay. For RNAseq analysis of iPSCs, iPSC-derived microglia and primary human microglia, the set of differentially expressed genes was identified from pairwise comparisons and heatmaps were generated using DEBrowser with clustering by Euclidean distance (Kucukural et al., 2019). Full characterization of human iPSC-derived microglia and additional details on the differentiation protocol will be published elsewhere (B.J.A., unpublished data).

### Primary Cell Cultures

#### **BMDM culture**

Mouse femur and tibia bones were dissected and briefly sterilized with 70% ethanol. The bones were washed twice with HBSS, then cracked in 10mL HBSS by mortar and pestle. The cell suspension was filtered through a 70µm cell strainer, spun at 300xg for 5 min, and supernatant was discarded. The cell pellet was resuspended in ACK Lysing Buffer (ThermoFisher A1049201) for 4 min at room temperature. 10mL RPMI-1640 (ThermoFisher) + 10% Hyclone FBS (GE Healthcare) + Penicillin-Streptomycin (ThermoFisher) was added to stop ACK lysis, then spun 300xg 5 min, and supernatant was discarded. Cells were resuspended in

RPMI-1640 + 10% Hyclone FBS + Penicillin-Streptomycin with 50ng/mL murine M-CSF (Life Technologies, PMC2044), counted and diluted to  $1 \times 10^6$  cells/mL, then plated on non-tissue culture treated Petri dishes. Three days after seeding, fresh murine M-CSF (50ng/mL) was added. Five days after seeding, cell culture media was aspirated and cells were washed once with PBS. Cells were resuspended in RPMI/FBS/Pen-Strep and harvested with a cell scraper. Cells were spun at 300xg for 5 min, supernatant was discarded, and cells were either diluted  $1 \times 10^6$  cells/mL for direct culture on tissue-culture treated plates, or frozen in RPMI/FBS/Pen-Strep + 10% DMSO for later use. TREM2 expression in *Trem2<sup>+/+</sup>*, *Trem2<sup>+/-</sup>*, and *Trem2<sup>-/-</sup>* BMDM was assessed by western blot of lysate from differentiated BMDM and immunostaining of TREM2 on live cells. Blots were stained with goat anti-TREM2 (1:1000, R&D systems AF1828) and mouse anti-beta-Actin (1:5,000, Sigma A2228). Live BMDM were stained with sheep anti-TREM2 (1:400, R&D systems) in DMEM + HEPES (25mM) + FBS (5%) for 1 hour on ice, then fixed with 4% PFA, 20 min at room temperature. Cells were blocked for 1hr RT with Rockland Blocking Buffer, then stained with donkey anti-sheep 488 (1:500, Invitrogen) and DAPI, and imaged on the Opera Phenix HCS System (PerkinElmer).

## METHOD DETAILS

### Immunofluorescence

Sagittal mouse hemibrains were flash frozen in liquid nitrogen after PBS perfusion and coronally cryosectioned at  $-20^{\circ}\text{C}$  with alternating 100 $\mu\text{m}$  (lipidomics) or 20 $\mu\text{m}$  (histology) widths using a Leica CM 1950 cryostat. 10 consecutive histological slide sets representing rostral to caudal brain regions were collected for each hemibrain and were frozen at  $-80^{\circ}\text{C}$ . Prior to staining, slides were thawed at room temperature until dry, then fixed with 4% paraformaldehyde (Electron Microscopy Sciences 15710) for 10 min. Slides were washed twice with PBS for 5 min, then blocked for 1 hr at room temperature with PBS + 0.3% Triton X-100 + 5% Normal Goat Serum (Vector Labs S-1000). Primary antibodies were diluted in blocking buffer and added to slide overnight at  $4^{\circ}\text{C}$ . Slides were washed 3X15 min in PBS and incubated with secondary antibodies diluted 1:1000 in blocking buffer for 2hr, room temperature. Slides were washed 3X15 min in PBS, dried at room temperature, and mounted with Fluoromount G (Southern Biotech 0100-01). Images of immunostained brain sections were captured with a 20x objective on a Zeiss AxioScan automated slide scanner driven by Zeiss Zen 2.3 software. All slides were imaged with the same exposure times and individual images from tissue sections were stitched together using Zen. APP staining was quantified both manually and automatically using Zen. In both cases, the dentate gyrus (DG)-CA1-CA2-CA3 region of the hippocampus (HC) was initially outlined manually, and the focus for quantification was the neuropil region of the HC as defined by sparse NeuN staining (Millipore MAB377, 1:100). For manual quantification, puncta of APP staining in HC neuropil were counted in blinded images from the selected HC regions. For automated staining, the automated analysis module in Zen was used to define neuropil within the selected HC region, and then to define regions of APP staining within neuropil by staining intensity and size. APP staining was then quantified by total object count, total area of APP staining, and total sum intensity of staining from each HC neuropil area. Finally, APP staining measures were normalized by dividing by total area of HC neuropil in the image.

### Neurofilament light detection

Mouse blood was collected into EDTA tubes (Sarstedt 201341102) with a capillary tube (Sarstedt 201278100), spun at 15,000xg for 7 min at  $4^{\circ}\text{C}$ , and the top plasma layer was transferred to a 1.5mL tube and stored at  $-80^{\circ}\text{C}$ . Frozen plasma samples were thawed on ice and diluted 10-fold and run on a SR-X (Quanterix) using the Simoa NF-light advantage kit (Quanterix 103186) according to the manufacturer's protocol.

### Fluorescence activated cell sorting (FACS)

To prepare a single cell suspension for sorting CNS cells, mice were perfused with PBS, brains dissected and processed into a single cell suspension according to the manufacturers' protocol using the adult brain dissociation kit (Miltenyi Biotec 130-107-677). Cells were Fc blocked and stained for flow cytometric analysis with Fixable Viability Stain BV510 to exclude dead cells (BD Biosciences 564406), CD11b-BV421 (BD Biosciences 562605), CD45-APC (BD Biosciences 559864), and ACSA-2-PE (Miltenyi Biotec 130-102-365). Cells were washed twice with Hibernate A (BrainBits LLC) and strained through a 100 $\mu\text{m}$  filter before sorting CD11b $^{+}$  microglia and ACSA-2 $^{+}$  astrocytes on a FACS Aria III (BD Biosciences) with a 100 $\mu\text{m}$  nozzle. Sorted cells were processed for downstream analyses using bulk RNAseq (CD11b $^{+}$ ), scRNAseq (CD11b $^{+}$  CD45 $^{\text{low}}$ ) or lipidomics (CD11b $^{+}$  CD45 $^{\text{low}}$ ). The vast majority of CD11b $^{+}$  cells were CD45 $^{\text{low}}$  with the CD11b $^{+}$  CD45 $^{\text{high}}$  cells representing less than 1% of the total live cells. We suspected these CD11b $^{+}$  CD45 $^{\text{high}}$  cells might be an infiltrating macrophage population and assessed the expression levels of cell-type specific markers via qPCR. We found that they expressed microglial markers, such as *Cx3cr1* and *Tmem119*, at much higher levels than macrophage markers (e.g., *Itgal*, *F10*, and *Gda*), suggesting they may also primarily be microglia and not infiltrated macrophages. In fact, recent scRNAseq work from others suggests negligible infiltration of peripheral monocytes and macrophages in the CPZ paradigm (Masuda et al., 2019).

### RNA isolation, qPCR, QuantSeq library preparation, and analysis

Live cells were sorted directly into RLT-plus buffer (QIAGEN, Hilden, Germany) with 1:100 beta-mercaptoethanol. RNA was extracted using the RNeasy Plus Micro Kit (QIAGEN, 74034) and resuspended in 14 $\mu\text{L}$  nuclease-free water. RNA quantity and quality were assessed with a RNA 6000 Pico chip (Agilent 5067-1513) on a 2100 Bioanalyzer (Agilent). For qPCR validation, 1-2 $\mu\text{L}$  RNA was

transcribed into cDNA using SuperScript IV (Invitrogen). Gene expression was assessed using Taqman probes for target genes on a QuantStudio 6 Flex (Applied Biosystems) and normalized to *Gapdh*. For QuantSeq library prep, RNA was processed using the QuantSeq 3' mRNASeq Library Prep Kit FWD for Illumina (Lexogen), following the ‘low-input’ protocol defined by the manufacturer. Libraries generated from young / aged wild-type mice also featured unique molecular identifiers (UMIs, Lexogen). Barcoded libraries were quantified using the NEBNext Library Quant Kit for Illumina (NEB, E7630S). All libraries were pooled in equimolar ratios into one sequencing library, which was quantified on a Bioanalyzer with a High Sensitivity DNA chip (Agilent, 5067-4626). 65 bp and 50 bp single-end reads from libraries with / without unique molecular identifiers, respectively, were generated in Illumina HiSeq 4000 lane at the UCSF Center for Advanced Technology.

Sequencing adapters were trimmed using skewer (Jiang et al., 2014) (version 0.2.2) with default parameters. Unique molecular identifiers (UMIs) were extracted from each read with the umi2index tool (Lexogen). Quality control of the trimmed reads was performed using FastQC (version 0.11.5: [www.bioinformatics.babraham.ac.uk/projects/fastqc](http://www.bioinformatics.babraham.ac.uk/projects/fastqc)). Reads were aligned to the mouse genome version GRCm38\_p6. A STAR index (version 2.5.3a) (Dobin et al., 2013) was built with the –sjdbOverhang = 50 argument. Splice junctions from Gencode gene models (release M17) were provided via the –sjdbGTFfile argument. STAR alignments were generated with the following parameters: –outFilterType BySJout, –quantMode TranscriptomeSAM, –outFilterIntronMotifs RemoveNoncanonicalUnannotated, –outSAMstrandField intronMotif, –outSAMattributes NH HI AS nM MD XS and –outSAMunmapped Within. Alignments were obtained with the following parameters: –readFilesCommand zcat –outFilterType BySJout –outFilterMultimapNmax 20 –alignSJoverhangMin 8 –alignSJDBoverhangMin 1 –outFilterMismatchNmax 999 –outFilterMismatchNoverLmax 0.6 –alignIntronMin ;20 –alignIntronMax 1000000 –alignMatesGapMax 1000000 –quantMode GeneCounts –outSAMunmapped Within –outSAMattributes NH HI AS nM MD XS –outSAMstrandField intronMotif –outSAMtype BAM SortedByCoordinate –outBAMcompression 6. Alignments sharing the same UMI and genomic coordinate were deduplicated using the collapse\_UMI\_bam tool (Lexogen). Gene level counts were obtained using featureCounts from the subread package (version 1.6.2) (Liao et al., 2014). Gene symbols and Entrez gene identifiers were mapped using Ensembl (version 91) via the biomaRt R package (version 2.34.2) (Durinck et al., 2005) using R (version 3.4.3). To identify differentially expressed genes linear models were fit using the limma Bioconductor package (Liu et al., 2015). Only genes with sufficiently large counts, as determined by edgeR’s “filterByExpr” function were included in the statistical analysis. TMM scaling factors for each sample were calculated with the “calcNormFactors” function (Robinson and Oshlack, 2010). We estimated the mean-variance relationship of log<sub>2</sub> transformed counts and derived observation-level weights with the “voom” function from the limma Bioconductor package (Liu et al., 2015). Linear models were fit with the “lmFit” and “eBayes” functions. Results were plotted using the ggplot2 R package (Wickham, 2016). Competitive gene set tests were performed using the “camera” algorithm from the limma R package (Wu and Smyth, 2012).

### Single cell RNAseq library preparation

Dissociated cells from (2) control diet *Trem2*<sup>+/+</sup> hemibrains and (2) *Trem2*<sup>+/+</sup>, (2) *Trem2*<sup>+/-</sup>, and (2) *Trem2*<sup>-/-</sup> 12-week CPZ treated hemibrains were processed and stained as described above. 30,000 live CD11b<sup>+</sup>/CD45<sup>low</sup> microglia were sorted from each hemibrain and (2) hemibrains per condition were pooled into PBS + 0.5% BSA to generate 4 total sequencing groups. Microglia were counted and diluted to 500,000 cells/mL in 70 µL and viability was verified to be > 70%. Single cell libraries were barcoded and prepared using Chromium Single Cell 3' Library Kit with v2 chemistry (10X Genomics, 120267) with a Chromium Controller (10X Genomics) at the Stanford Functional Genomics Facility. ScRNASeq libraries were sequenced using a NovaSeq S4 (Illumina) at the UCSF Center for Advanced Technology.

### Single cell RNAseq data processing

The fastq files from each dataset were individually processed using Cell Ranger (10X Genomics, v2.1). The “raw\_gene\_bc\_matrices” directories from these runs served as the starting point for all subsequent quality control, filtering, and downstream analyses. These steps were performed using a combination of the DropletUtils, scater (McCarthy et al., 2017) and scran (Lun et al., 2016b) Bioconductor (v3.8) packages. Experiments were independently quality controlled and filtered by removing low quality droplets. First, droplets containing only ambient levels of RNA were removed. We then calculate per cell: (i) the number of UMIs; (ii) number of genes detected; (iii) fraction of reads that map to ribosomal proteins; and (iv) fraction of reads that map to the mitochondrial genome. Cells that are outliers in any of these metrics (> 2-3 median absolute deviations too low for (i) and (ii), too high for (iii) and (iv)) are removed. Read counts were normalized using a deconvolution strategy for scaling normalization of sparse count data (Lun et al., 2016a). All downstream analyses were performed using the 4,895 genes that were identified with positive components of biological variance (i.e., higher variance than the assumed technical Poisson noise) as implemented in the “decomposeVar” method in the scran package.

### Single cell RNAseq cluster and expression analysis

PCA was performed on the log<sub>2</sub> normalized gene expression matrix, and the top twenty-one principal components were retained. A shared nearest neighbor graph (Xu and Su, 2015) was built over the data in PC-space followed by community detection using the Louvain method (Blondel et al., 2008) to assign cells to one of eight clusters. Marker genes per cluster were identified by exhaustively performing pairwise Wilcoxon tests, as implemented in the scran package. Briefly, the expression level of each gene within a cluster was tested against each of the other seven clusters, individually. The p values were combined using Simes’ method (Simes, 1986) to provide a final p value for the gene’s differential expression status per cluster, which were then adjusted to correct for multiple testing

using the Benjamini–Hochberg method (Benjamini and Hochberg, 1995). Effect sizes for each comparison are calculated as “overlap proportions” i.e., the probability that a cell selected at random within the source cluster has higher expression of gene X than a random cell in the query cluster. Overlap proportions (Wilcoxon effect sizes) are averaged over all pairwise comparisons to provide a final effect size for the gene within the cluster. Finally, marker genes per cluster were extracted by identifying the genes with an FDR < 0.05 and averaged overlap proportions lower than 0.4 or greater than 0.6. Although cluster 3 showed a mild increase in abundance under CPZ treatment (~1.2% of *Trem2*<sup>+/+</sup> cells with control diet, to ~2.7% *Trem2*<sup>+/+</sup> cells with CPZ diet, ~2.5% *Trem2*<sup>+-</sup> cells with CPZ diet, ~2.0% *Trem2*<sup>-/-</sup>, it was comprised of very few cells and closer analysis suggests this cluster of cells to be lower quality cells that slipped through our aforementioned quality control. Gene ontology analysis of the top upregulated marker genes within this cluster are enriched for mitochondrial cellular compartments, such as “inner mitochondrial membrane protein complex” (GO:0098800, FDR: 0.01), “mitochondrial membrane part” (GO:0044455, FDR: 0.02), among others (Ilicic et al., 2016).

### Brain sample collection and preparation for LCMS analysis

Sagittal mouse hemibrains were flash frozen in liquid nitrogen after PBS perfusion and coronally cryosectioned at –20°C with alternating 100 µm (for lipid analysis) or 20 µm (histology) widths. Two 100µm sections from matched forebrain regions containing the corpus callosum were placed in a 1.5mL lo-bind tube (Eppendorf) containing a 3 mm stainless steel bead (QIAGEN) with 200 µL of LCMS grade methanol containing internal standards. Tubes were lysed using TissueLyser (QIAGEN) for 1 min at 25Hz and 4°C. 20 µL of sample was removed for protein concentration measurements using the bicinchoninic acid (BCA) assay (Pierce, Rockford, IL, USA). Lysate was spun for 20 min, 18,000 xg at 4°C. Supernatant was transferred to glass vials for further LCMS analyses.

### FACS lipid extraction

Dissociated cells were stained according to above FACS protocols, except all staining buffers contained PBS + 1% fatty acid-free BSA (Sigma; A7030). 400µL methanol containing internal standards were added to 2mL lo-bind tubes (Eppendorf). After sorting, total volume was adjusted to 800µL with deionized water (Milli-Q). Samples were vortexed 5 min, 2500 rpm at room temperature. 800µL methyl tertiary-butyl ether (MTBE) was added and samples were vortexed 5 min, 2500 rpm at room temperature, then spun at 21000xg, 10 min at 4°C. 600 µL MTBE supernatant was transferred to glass LCMS vials and dried under nitrogen gas. Samples were resuspended in 100 µL of methanol for further LCMS analyses.

### CSF sample collection and preparation for LCMS analysis

Mice were anesthetized using 2.5% Avertin/tert-amyl alcohol. After sedation, a sagittal incision was made at the back of the animal’s skull to expose the cisterna magna and a needle attached to a glass capillary tube was used to puncture the cisterna magna to collect CSF. CSF was transferred to 0.5mL lo-bind tubes (Eppendorf) and spun at 12,000rpm for 10 min, 4°C. 2µL of supernatant was transferred to glass LCMS vials and 50µL methanol containing internal standards was added before LCMS analyses.

### LCMS analysis of lipids

Lipid analyses were performed by liquid chromatography (Nexera X2, Shimadzu Scientific Instrument, Columbia, MD, USA) coupled to electrospray mass spectrometry (QTRAP 6500+, Sciex, Framingham, MA, USA) or liquid chromatography (ACQUITY I-Class Plus UPLC FTN, Waters Corporation, Milford, MA USA) coupled to electrospray mass spectrometry (XEVO TQ-S Micro, Waters). For each analysis, 5 µL of sample was injected on an ACQUITY UPLC BEH C18 1.7 µm, 2.1 × 100 mm column (Waters) using a flow rate of 0.25 mL/min at 55°C. For positive ionization mode, mobile phase A consisted of 60:40 acetonitrile/water (v/v) with 10 mM ammonium formate + 0.1% formic acid; mobile phase B consisted of 90:10 isopropyl alcohol/acetonitrile (v/v) with 10 mM ammonium formate + 0.1% formic acid. For negative ionization mode, mobile phase A consisted of 60:40 acetonitrile/water (v/v) with 10 mM ammonium acetate + 0.1% acetic acid; mobile phase B consisted of 90:10 isopropyl alcohol/acetonitrile (v/v) with 10 mM ammonium acetate + 0.1% acetic acid. The gradient was programmed as follows: 0.0–8.0 min from 45% B to 99% B, 8.0–9.0 min at 99% B, 9.0–9.1 min to 45% B, and 9.1–10.0 min at 45% B. Electrospray ionization was performed in either positive or negative ion mode. For the QTRAP 6500+ we applied the following settings: curtain gas at 30 V; collision gas was set at medium; ion spray voltage at 5500 V (positive mode) or –4500V (negative mode); temperature at 250°C (positive mode) or 600°C (negative mode); ion source Gas 1 at 50 psi; ion source Gas 2 at 60 psi; declustering potential at 80 V; entrance potential at 10 V; and collision cell exit potential at 12.5 V. For the XEVO TQ-S Micro we applied the following settings: capillary voltage at 2.0 kV; source temperature at 150°C; desolvation temperature at 400°C; desolvation gas flow at 1000 L/hr; cone gas flow at 25 L/hr; cone voltage at 40 V; nebulizer gas at 7 bar. Data acquisition was performed in multiple reaction monitoring mode (MRM) with the collision energy (CE) values reported in Table S1. Lipids were quantified using a mixture of non-endogenous internal standards as reported in Table S1. Quantification was performed using MultiQuant 3.02 (Sciex) and TargetLynx 4.2 (Waters). Metabolites were normalized to either total protein amount or cell number.

BMP species were analyzed by liquid chromatography (Nexera X2, Shimadzu Scientific Instrument) coupled to electrospray mass spectrometry (Sciex 6500+ QTRAP, Sciex). For each analysis, 5 µL of sample was injected on a ACQUITY UPLC BEH amide 1.7 µm, 2.1 × 150 mm column (Waters) using a flow rate of 0.40 mL/min at 55°C. Mobile phase A consisted of water with 10 mM ammonium formate + 0.1% formic acid. Mobile phase B consisted of acetonitrile with 0.1% formic acid. The gradient was programmed as follows: 0.0–1.0 min at 95% B; 1.0–7.0 min to 50% B; 7.0–7.1 min to 95% B; and 7.1–12.0 min at 95% B. Electrospray ionization was performed in the negative-ion mode applying the following settings: curtain gas at 30 psi; collision gas was set at medium; ion spray

voltage at 5200V; temperature at 600°C; ion source Gas 1 at 50 psi; Gas 2 at 60 psi; CE at -50V, collision cell exit potential at -15V; declustering potential at -60V; entrance potential at -10V. Data acquisition was performed using Analyst 1.6 (Sciex) in MRM mode (**Table S1**). Quantification was performed using MultiQuant 3.02 (Sciex).

Glucosylceramide (GlcCer), galactosylceramide (GalCer), glucosylsphingosine (GlcSph) and galactosylsphingosine (GalSph) analyses were performed by liquid chromatography (Nexera X2, Shimadzu Scientific Instrument) coupled to electrospray mass spectrometry (QTRAP 6500+, Sciex). For each analysis, 10 $\mu$ L of sample was injected on a HALO HILIC 2.0  $\mu$ m, 3.0  $\times$  150 mm column (Advanced Materials Technology, Wilmington, DE, USA) using a flow rate of 0.45 mL/min at 45°C. Mobile phase A consisted of 92.5/5/2.5 acetonitrile/ isopropyl alcohol/water with 5 mM ammonium formate and 0.5% formic acid. Mobile phase B consisted of 92.5/5/2.5 water/ isopropyl alcohol/acetonitrile with 5 mM ammonium formate and 0.5% formic acid. The gradient was programmed as follows: 0.0–3.1 min at 100% B, 3.2 min at 95% B, 5.7 min at 85% B, hold to 7.1 min at 85% B, drop to 0% B at 7.25 min and hold to 8.75 min, ramp back to 100% at 10.65 min and hold to 11 min. Electrospray ionization was performed in the positive-ion mode applying the following settings: curtain gas at 25 psi; collision gas was set at medium; ion spray voltage at 5500V; temperature at 350°C; ion source Gas 1 at 55 psi; ion source Gas 2 at 60 psi. Data acquisition was performed in MRM mode with the transitions and CE values reported in **Table S1**; declustering potential at 45V; entrance potential at 10V; and collision cell exit potential at 12.5V. Lipids were quantified using a mixture of internal standards as reported in **Table S1**. Quantification was performed using MultiQuant 3.02 (Sciex).

### Liposome preparation

70 molar percent DOPC (1,2-dioleoyl-sn-glycero-3-phosphocholine, Avanti Polar Lipids) and 30 molar percent of one test lipid were combined in chloroform in a glass vial and dried under a stream of N2 gas for 1-2h, or until completely dry. Test lipids included sulfatide (Avanti), POPS (Avanti), SM (Avanti), PI (Avanti), GalCer (Avanti), PE (Echelon Biosciences), and free cholesterol (Echelon Biosciences). The lipid mixture was re-suspended in HBSS (1-2mg/mL final lipid concentration) and vortexed for 2-3 min. Subsequently, the lipid suspension was bath sonicated for 10 minutes. For surface plasmon resonance experiments, liposomes were extruded 10 times using an Avanti mini-extruder constructed with one 100nm pore size membrane to form small unilamellar vesicles.

### pSYK AlphaLISA

Activation of TREM2-dependent pSYK signaling was measured using a commercial AlphaLISA assay (PerkinElmer). HEK293 cells: Two days before the experiment, HEK293 cells stably overexpressing TREM2 and DAP12 were plated at 40,000 cells/well on 96 well poly-D-lysine-coated plate. Differentiated human macrophage and BMDM were plated at 100,000 cells/well on tissue-culture treated 96-well plates. Cells were washed once with HBSS, then 50 $\mu$ L of liposome mixture was added per well. For competition experiments, hTREM2-ECD or TREM1-his (Novoprotein Scientific) was incubated with liposomes for 1 hour at room temperature before adding to cells. 5 $\mu$ g/mL human-specific mouse anti-TREM2 (Abnova) or 15 $\mu$ g/mL mouse-specific sheep anti-TREM2 (R&D Systems) was added to each experiment as a positive control with side-by-side isotype controls, 5 $\mu$ g/mL mouse IgG3 (R&D Systems) and 15 $\mu$ g/mL polyclonal sheep IgG (R&D Systems), respectively. The cell plate was then transferred to a 37°C incubator for 5 minutes. The liposome solution was discarded and 40 $\mu$ L lysis buffer (Cell Signaling Technologies, CST) was added. Lysate was incubated at 4°C for 30 min, then either frozen at -80°C or immediately carried forward to the alpha-LISA assay. Lysates were assayed using the standard protocol for the PerkinElmer pSYK AlphaLISA kit. 10 $\mu$ L of lysate/well was transferred to a white opaque 384 well Optiplate (PerkinElmer). 5 $\mu$ L of Acceptor Mix (containing the working solution of acceptor beads) was added per well followed by sealing plates with foil and incubating 1 hour at room temperature. 5 $\mu$ L of Donor Mix (containing the working solution of donor beads) was added to each well under reduced light conditions. Plates were again sealed and incubated 1 hour at room temperature. Plates were read using AlphaLISA settings on a PerkinElmer EnVision plate reader.

### Recombinant purification of His tagged hTREM2 and hTREM2 R47H ECD

Expi293F medium was harvested 96 hr post transfection and supplemented with 1M imidazole pH 8.0 to a final concentration 10 mM, filtered, then loaded on to HisPur Ni-NTA Resin equilibrated with load buffer (20 mM Tris pH 8.0, 150 mM NaCl and 10 mM Imidazole). Nonspecifically bound proteins were washed with load buffer supplemented with 50 and 100 mM imidazole and TREM2 ecto domain was eluted with 20 mM Tris pH 8.0, 150 mM NaCl and 200 mM Imidazole. Eluted protein was pooled and subjected to size exclusion chromatography onto a HiLoad Superdex 75 16/600 column using 1X PBS as the running buffer. Elute fractions were analyzed by SDS-PAGE and further characterized by analytical size exclusion chromatography and the intact protein mass determination.

### Lipid binding analysis using surface plasmon resonance (SPR)

The binding analysis was performed using Series S Sensor chip L1 and Biacore T200 instrument (GE Healthcare) at 25°C. Before coating with lipids, the sensor surfaces were washed with 1 minute injection of 40  $\mu$ M 3-[3-cholamidopropyl]dimethylammonio]-1-propanesulfonate (CHAPS) and 40  $\mu$ M of  $\beta$ -octylglucoside at a flow rate of 30  $\mu$ l/min. Residual detergent on the sensor surfaces was washed away by 30 s injection of 30% ethanol.

1 mg/ml Sulfatide/DOPC or PS/DOPC small unilamellar vesicles were injected for 15 minutes at 5  $\mu$ l/min over the second flow cell. First flow cell was coated with DOPC and served as a reference surface. Loosely bound vesicles were washed away with two short pulses (15 s) of 10 mM NaOH at 30  $\mu$ l/min followed by injection of 0.1 mg/ml bovine serum albumin for 3 minutes to block

poorly-coated surface. Recombinant hTREM2-ECD or hTREM2-R74H-ECD proteins were diluted in PBS (0, 0.19, 0.56, 1.7, 5, and 15  $\mu$ M) and injected over both flow cells for 60 s at 30  $\mu$ L/min, and dissociation was monitored for additional 2 minutes. Between each measurement the lipids surface was regenerated by injection of 10 mM NaOH. Steady-state affinities were obtained by fitting the response at equilibrium against the concentration using Biacore T200 Evaluation Software v3.1.

### Myelin purification and phagocytosis

Myelin was purified from wild-type C57BL/6 mouse brain (Jackson Laboratories) using previously described methods (Safaiyan et al., 2016). Each mouse brain was dissected and placed in 1.2mL cold lysis buffer (10mM HEPES, 5mM EDTA, 0.3M sucrose, cOmplete protease inhibitor tablet (Roche, 4693159001), chopped into fine pieces with a razor blade, then dissociated via Dounce homogenization. Homogenate was transferred to Ultra-Clear tubes (Beckman 344060) and an equal volume (1.2mL/brain) of 0.32M sucrose was carefully added underneath with a sterilized Pasteur pipette, then an equal volume (1.2mL/brain) of 0.85M sucrose was added underneath both layers. Samples were spun at 75,000 g, 4°C, 30min in a SW 40 Ti rotor in a Optima XPN-80 ultracentrifuge (Beckman) with low acceleration and deceleration. Myelin was carefully removed at the 0.32M/0.85M sucrose interface and resuspended in 10mL distilled water, placed into an ultracentrifuge tube, then spun at 75,000 g, 4°C, 15min with max acceleration and deceleration. The pellet was resuspended in 10mL distilled water, then spun at 12,000 g, 4°C, 10min with max acceleration and deceleration two times. The pellet was resuspended in lysis buffer and all steps were repeated to obtain pure myelin. Following purification, myelin was resuspended in PBS and adjusted to 1mg/mL protein concentration using the DC Protein Assay Kit 2 (BioRad, 5000112). Fractions of purified myelin were labeled using the pHrodo Red Microscale Labeling Kit (ThermoFisher, P35363) as per manufacturer recommendations. BMDM were plated in RPMI/10% FBS/Pen-Strep at a density of 100,000 cells per well in tissue culture treated 96 well plates (CellCarrier, PerkinElmer) supplemented with 5ng/mL mouse M-CSF. As a negative control, 10 $\mu$ M Cytochalasin D was added to cells 1 hr before myelin and retained throughout uptake assays. Cells were prestained with CellMask Deep Red Plasma Membrane Stain (1:5000, ThermoFisher C10046) and NucBlue Live ReadyProbes Reagent (2 drops per 1mL, ThermoFisher R37605) in cell culture medium for 10 min, 37°C. pHrodo-myelin was diluted to 5 $\mu$ g/mL in cell culture medium and bath sonicated for 1 min, then added to cells for 2-4 hr and imaged live (5% CO<sub>2</sub>, 37°C) at 15-30 min intervals on an Opera Phenix HCS System (PerkinElmer). Individual cells were identified by nuclear and cell membrane stain, then pHrodo uptake intensity was quantified per cell per well using Harmony HCA Software (PerkinElmer).

### Lipid challenge experiments in BMDMs and human iPSC-derived microglia

BMDM (100,000/well) were plated on PDL-coated 96-well plates in RPMI/10% FBS/Pen-Strep with noted M-CSF concentrations. After 24hr at 37°C, purified myelin (25 $\mu$ g/mL or 50 $\mu$ g/mL) or oxLDL (Thermo Fisher L34357, 50 $\mu$ g/mL) was spiked into the wells. For experiments with oxLDL, a second addition of the same amount of oxLDL was spiked into the wells 24hr after the first addition. In experiments with ACAT inhibitor, 500nM ACAT inhibitor K604 or vehicle control was spiked together with the first lipid dose. K604 was synthesized according to protocols published in patent US 2004/0038987 A1. Human iPSC-derived microglia were plated at 30,000/well on 96-well plates in IMDM/10% FBS/1% Pen-Strep with 20ng/mL human IL-3 (Peprotech 200-03), 20ng/mL human GM-CSF (Peprotech 300-03), and 20ng/mL human M-CSF (Peprotech 200-25). After 24hr at 37°C, purified myelin (25 $\mu$ g/ $\mu$ L) was spiked into the wells, with or without 500nM K604 or 10 $\mu$ M LXR agonist GW3965. After 48hr-72hr at 37°C of lipid treatment, cells were collected or imaged. For Nile Red imaging of BMDMs, the supernatant was removed and cells were incubated at 37°C for 30 min in live cell imaging buffer (Life Technologies, A14291DJ) containing 1 $\mu$ M Nile Red (Thermo Fisher N1142) and 1 drop/mL of NucBlue (Thermo Fisher R37605). After incubation, the staining solution was removed and cells were fixed in 4% paraformaldehyde. The cells were then imaged using 568 and DAPI illumination settings on an Opera Phenix HCS System (PerkinElmer). Lipid spots were analyzed using a spot-finding algorithm on Harmony HCA Software (PerkinElmer). For LCMS, cells were washed with PBS on ice. 70 $\mu$ L of a 9:1 methanol:water solution containing internal standards was added to the cells in the 96-well plate. The plate was agitated on a shaker at 4°C, 1200rpm for 20 min, then spun down for 5 min at 300xg. 50 $\mu$ L of supernatant was transferred to glass vials for further LCMS analyses. To account for differences in cell number, lipid concentrations were normalized to the ratio of DAPI-positive cells in each condition to the DAPI-positive cells in the *Trem2<sup>+/+</sup>*, vehicle-treated condition.

### QUANTIFICATION AND STATISTICAL ANALYSIS

Statistical comparisons for lipidomic heatmaps were performed using MetaboAnalyst 4.0 (<https://www.metaboanalyst.ca>) (Chong et al., 2018). For TREM2 samples, missing values (forebrain: 0%, CSF: 0.4%, microglia: 3.2%, astrocytes: 6.4%) were replaced by the mean of all samples for a given lipid species, then analyzed as two-factor independent samples and log transformed. ApoE samples were analyzed via ANOVA on log transformed data. Genotype and treatment comparisons for individual lipid species were conducted using Prism (Graphpad). Two-way ANOVA was run separately for 5 and 12 week CPZ conditions and reported statistics are from significant interactions between genotype and treatment. Tukey posthoc test was used to distinguish which genotype contributed to the reported interactions.

For LCMS analyses of BMDM and human iPSC-derived microglia, differential abundance between experimental groups was identified by fitting the following ANOVA model for each lipid: log10(abundance) ~ treatment + genotype + challenge:genotype + batch. Each LCMS plot in Figures 7 and S7 shows the batch-adjusted mean and its 95% confidence interval for each group, which includes

3 biological replicates. Significant baseline differences between genotypes (main effect) are indicated as #  $p < 0.05$ , ##  $p < 0.01$  and ###  $p < 0.001$ . Significant drug treatment effects were identified within each genotype by performing a paired t test on the log<sub>10</sub> transformed abundances comparing the Myelin / Myelin + inhibitor groups and are indicated as \*  $p < 0.05$  and \*\*  $p < 0.01$ . Significant drug treatment effects are identified within each genotype by paired t test on the log<sub>10</sub> transformed abundances comparing myelin / myelin + inhibitor groups (n = 3 biological replicates): \*  $p < 0.05$  and \*\*  $p < 0.01$ .

For bulk microglia QuantSeq and scRNAseq experiments, statistical methods are explained in respective methods sections. All other statistics were conducted with Prism (GraphPad). Statistical testing criteria and significance for each experiment are noted in the main text and figure legends.

#### DATA AND CODE AVAILABILITY

Raw and processed RNA-sequencing data are available via the NCBI GEO repository under accession GEO: GSE130627.